Biophysical Journal
Article

Biophysical Society

Optimal cell traction forces in a generalized motor-clutch model

Roberto Alonso-Matilla,[1,2,3] Paolo P. Provenzano,[1,2,3,4,5,6] and David J. Odde[1,2,3,4,*]
[1]Department of Biomedical Engineering, University of Minnesota, Minneapolis, Minnesota; [2]University of Minnesota Physical Sciences in Oncology Center, Minneapolis, Minnesota; [3]University of Minnesota Center for Multiparametric Imaging of Tumor Immune Microenvironments, Minneapolis, Minnesota; [4]Masonic Cancer Center, University of Minnesota, Minneapolis, Minnesota; [5]Department of Hematology, Oncology, and Transplantation, University of Minnesota, Minneapolis, Minnesota; and [6]Stem Cell Institute, University of Minnesota, Minneapolis, Minnesota

ABSTRACT Cells exert forces on mechanically compliant environments to sense stiffness, migrate, and remodel tissue. Cells can sense environmental stiffness via myosin-generated pulling forces acting on F-actin, which is in turn mechanically coupled to the environment via adhesive proteins, akin to a clutch in a drivetrain. In this "motor-clutch" framework, the force transmitted depends on the complex interplay of motor, clutch, and environmental properties. Previous mean-field analysis of the motor-clutch model identified the conditions for optimal stiffness for maximal force transmission via a dimensionless number that combines motor-clutch parameters. However, in this and other previous mean-field analyses, the motor-clutch system is assumed to have balanced motors and clutches and did not consider force-dependent clutch reinforcement and catch bond behavior. Here, we generalize the motor-clutch analytical framework to include imbalanced motor-clutch regimes, with clutch reinforcement and catch bonding, and investigate optimality with respect to all parameters. We found that traction force is strongly influenced by clutch stiffness, and we discovered an optimal clutch stiffness that maximizes traction force, suggesting that cells could tune their clutch mechanical properties to perform a specific function. The results provide guidance for maximizing the accuracy of cell-generated force measurements via molecular tension sensors by designing their mechanosensitive linker peptide to be as stiff as possible. In addition, we found that, on rigid substrates, the mean-field analysis identifies optimal motor properties, suggesting that cells could regulate their myosin repertoire and activity to maximize force transmission. Finally, we found that clutch reinforcement shifts the optimum substrate stiffness to larger values, whereas the optimum substrate stiffness is insensitive to clutch catch bond properties. Overall, our work reveals novel features of the motor-clutch model that can affect the design of molecular tension sensors and provide a generalized analytical framework for predicting and controlling cell adhesion and migration in immunotherapy and cancer.

SIGNIFICANCE Adherent cells produce mechanical forces on their environment to mediate cell adhesion and signaling in development and disease progression. Despite recent progress, cell-generated force measurements across a wide range of extracellular stiffnesses and cell states have faced numerous technical challenges. Our mean-field study provides a new generalized analysis of regulation of force transmission by modulation of cellular components and extracellular rigidity. Here, we identify the existence of an intermediate stiffness of cell adhesion molecules for maximum force transmission and find that maximal force transmission on rigid environments depends on myosin motor properties. The generalized analysis provides important insights to aid design of novel molecular tension sensors and therapeutic strategies for cancers and other diseases.

INTRODUCTION

Cell migration plays a pivotal role in many biological processes, such as embryonic morphogenesis, wound healing, and cancer progression. A major challenge in cell biology is to understand how cells within an organism migrate through different environments. During migration, cells undergo a complex series of events that occur in a highly dynamic fashion (1,2). According to the motor-clutch hypothesis (3), cells start off the migration cycle by the extension of cell membrane protrusions driven by actin polymerization, followed by the formation of complex

Submitted February 20, 2023, and accepted for publication July 17, 2023.
*Correspondence: oddex002@umn.edu
Editor: Alex Mogilner.
https://doi.org/10.1016/j.bpj.2023.07.012
© 2023 Biophysical Society.
This is an open access article under the CC BY-NC-ND license (http://creativecommons.org/licenses/by-nc-nd/4.0/).

adhesion structures and generation of traction forces (4). Adhesion complexes function as molecular clutches by mechanically coupling the actin cytoskeleton to the extracellular substrate via membrane-bound receptors. Clutches cooperatively resist the forces arising from the rearward flow of actin filaments and transmit them to the substrate, allowing the cell to move forward (5–7). The flow of F-actin away from the leading edge, known as retrograde flow, emerges as actin filaments are subject to rearward forces produced by the leading-edge membrane due to actin polymerization (8) as well as by myosin motors as they bind and pull filaments away from the leading edge (9). Actin polymerization, adhesion formation, and myosin forces are therefore mechanically coordinated allowing cells to migrate and explore their extracellular environment.

How cells sense and respond to the mechanical features of their environment has been the focus of many studies (10–15). According to the motor-clutch model, coupling between the extracellular substrate and the actin cytoskeleton by molecular clutches permits the transmission of actomyosin-generated forces to the substrate, allowing cells to sense the mechanical properties of the environment (2,16). The motor-clutch model exhibits rigidity sensing, which emerges from load-dependent clutch-bond dissociation rates and load-dependent myosin motor force generation (2,10,17,18), and captures the reported biphasic dependence of cell migration on substrate adhesion strength, first postulated by DiMilla et al. (19) and later confirmed experimentally (20,21). Cell motility (12,21–27) and traction forces (12,13) have been reported to exhibit a biphasic dependence on substrate adhesivity/stiffness. Some cells, however, deviate from the biphasic force-rigidity relationship at physiological substrate stiffnesses through force-mediated clutch reinforcement (14,28). Also, some cells produce higher traction forces on stiffer substrates (29–32), whereas other cells produce higher traction forces on softer substrates (2). Together, these studies suggest the existence of an optimal substrate stiffness for maximal traction force, as observed experimentally (12,14).

Previous mean-field model studies addressed the production of traction forces on infinitely rigid substrates (33–36) and in compliant linearly elastic (17) and viscoelastic (37) substrates. Motor-clutch studies (2,10,17) identified the existence of three different traction force production regimes: a stalled regime characterized by clutch-dominated protrusions, a balanced regime characterized by a motor-clutch balanced protrusion, and a free-flowing regime characterized by motor-dominated protrusions. In this study, we introduce a mean-field representation of the motor-clutch model (2) with the aim of gaining a more general theoretical understanding of traction force production from individual cellular protrusions on elastic substrates that does not assume that motors and clutches are balanced. In addition, we included force-dependent clutch reinforcement (14,28) and catch bonding (38,39). In particular, we apply scaling analysis to our model with the purpose of deriving an analytical expression for the optimum substrate stiffness (i.e., the substrate stiffness that maximizes traction forces). In this work, we relax the adjustable parameter assumption made in (17) and derive a more general expression for the optimum substrate stiffness that is applicable to all motor-clutch ratio regimes. Our generalized mean-field model results allow us to identify the existence of an optimum clutch stiffness for maximal cellular traction force. In addition, we capture a biphasic dependence of force transmission on motor activity on rigid substrates and identify an intermediate myosin load-free velocity parameter for maximum traction force. Finally, we find that load-dependent clutch reinforcement can significantly shift the optimum substrate and clutch stiffnesses to larger values, increasing substantially the traction force produced by protrusions that display load-and-fail dynamics, whereas catch bond properties can modulate force transmission but do not affect the optimum substrate stiffness for maximum force. Our mean-field approach additionally allowed us to carry out an in-depth exploration of the distribution of clutch force states during the loading cycle as a function of all parameters grouped together to define new dimensionless variables and parameters.

MATERIALS AND METHODS

The developed mean-field theory is a generalization of the model by Bangasser and Odde (17), where a probability that each existing clutch in the protrusion is mechanically linking the actin cytoskeleton and the extracellular substrate was introduced. In this work, we introduce a multibond probability density of finding any clutch with a given extension at any instantaneous time and derive its conservation equation (see supporting material). Our approach relaxes the previous assumption that motors and clutches are balanced, without requiring an unknown parameter to define the optimum, and analytically investigates previously uncharacterized optimality of clutch stiffness, clutch catch bond behavior, and load-dependent clutch-bond reinforcement behavior, the latter two of which are common features of motor-clutch cellular systems. The present treatment allowed us to make a more complete and generalized analysis of cellular force transmission and further explored the entire motor-clutch model parameter space.

According to the motor-clutch hypothesis, myosin motors bind and pull actin filaments retrogradely away from the leading edge producing retrograde forces (Fig. 1 *A*). Forces on actin filaments are transmitted to the extracellular matrix through protein complexes, commonly called clutches, that mediate the production of traction forces on the surrounding compliant substrate allowing the cell body to propel forward. Molecular clutches bind—that is, couple—actin filaments to the compliant substrate in an unloaded state at a force-independent rate k_{on} (see Table 1 for a summary of all parameters and estimated base values). Clutches form slip bonds and unbind with an effective dissociation rate that increases exponentially with force according to Bell's law $k_{off}^{load} = k_{off}\, e^{|F_c|/F_b}$ (52), where k_{off} is the unloaded clutch dissociation rate, F_b is the characteristic bond rupture force, and F_c is the force on the clutch. The simplest motor-clutch description is to consider molecular clutches and the surrounding substrate as Hookean elastic materials. Accordingly, the clutch force is given by Hooke's law $F_c = \kappa_c x_c$, where κ_c is the effective clutch stiffness and x_c is the clutch

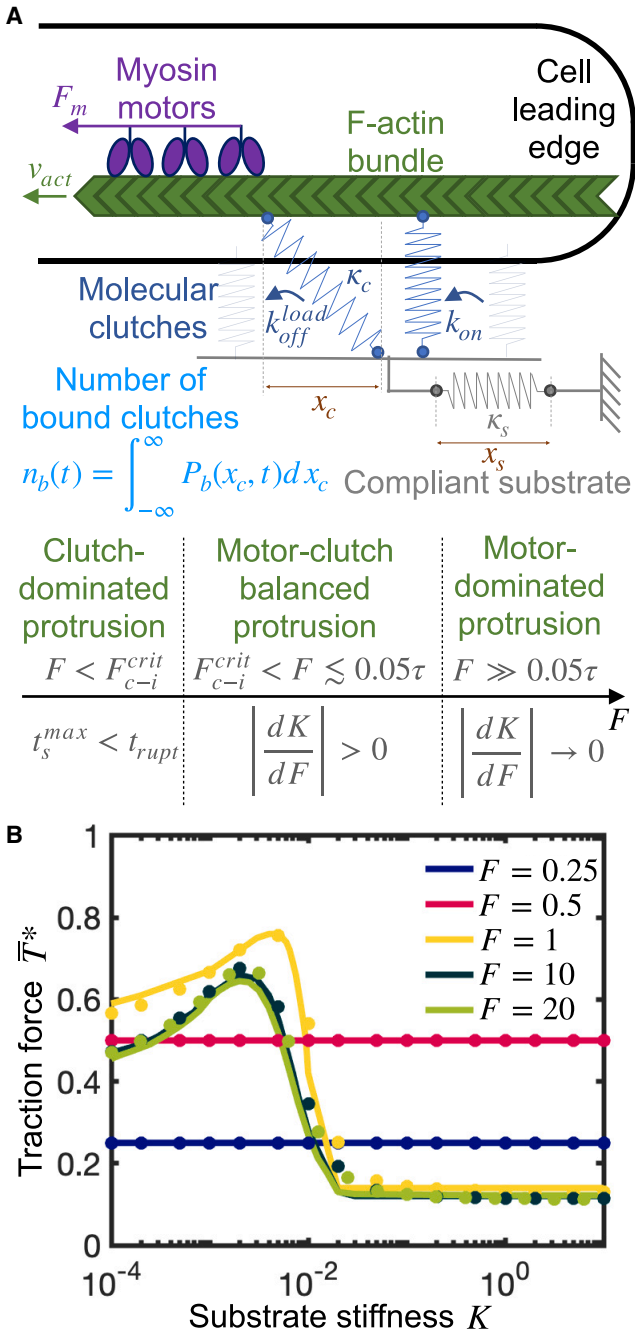

FIGURE 1 Traction force production of individual cellular protrusions exhibit three different regimes: a motor-dominated regime, an intermediate motor-clutch balanced regime, and a clutch-dominated regime. Mean-field motor-clutch model captures force transmission sensitivity to substrate compliance. (*A*) Sketch of the model and required conditions for the protrusion to operate at each traction force production regime. (*B*) Dimensionless time-averaged traction force $\overline{T}^* = \overline{T}/n_c F_b$ as a function of the dimensionless substrate stiffness K for various values of the myosin activity parameter F. Protrusions can belong to three different regimes: a motor-dominated regime characterized by the existence of an optimum stiffness for maximal traction that is largely independent of myosin activity (F = 10 and F = 20), a clutch-dominated regime characterized by stiffness-independent traction forces (F = 0.25 and F = 0.5), and an intermediate regime characterized by an optimum stiffness sensitive to motor activity (F ∼ 1). The three regimes are analyzed in detail in the main text. Solid lines are the numerical solution of the mean-field model Eqs. 3 and 4, and circular solid symbols are the mean statistics obtained from the numerical solution of the stochastic model. There is a very good agreement between the mean-field model solution and stochastic model solution. Parameter values: $\tau = 10, \omega = 2000$. To see this figure in color, go online.

extension, measured with respect to its resting value. To study clutch elongation dynamics, we introduce a probability density function $P_b(x_c, t)$ of finding a bound clutch with elongation x_c at time t. Conservation of P_b implies (see supporting material):

$$\frac{\partial P_b}{\partial t} = k_{on}(n_c - n_b)\delta(x_c) - k_{off}^{load} P_b - v_e \frac{\partial P_b}{\partial x_c}. \quad (1)$$

The first term on the right-hand side (RHS) of Eq. 1 corresponds to the rate of change of the probability density due to clutch binding kinetics, where $\delta(x_c)$ is the Dirac delta function, which enforces clutches to engage in an unloaded configuration. The number of bound clutches that mechanically connect the cytoskeletal filaments with the substrate is denoted by $n_b(t)$, and n_c is the total number of available clutches in the cellular protrusion. The second term on the RHS of Eq. 1 is the rate of change of the probability density due to clutch dissociation kinetics, and the last term of Eq. 1 accounts for the rate of change of the probability density due to force-mediated clutch extension, where the clutch elongation rate is $v_e = v_{act} - dx_s/dt$, where v_{act} is the actin filament velocity and dx_s/dt is the substrate deformation rate. We therefore follow the standard motor-clutch view and assume that all bound clutches equally deform at any time, where the actin-binding domains of clutches move at the actin retrograde flow velocity v_{act} and their substrate-binding domains move rigidly with the substrate. Furthermore, myosin motors obey a linear force-velocity relation; thus, the total force exerted by myosin motors on the actin filament bundle is $F_{act} = n_m F_m(1 - v_{act}/v_u)$, where n_m is the total number of myosin motors in the protrusion, F_m is the stall force exerted by one myosin motor, and v_u is the load-free velocity of myosin motors. For convenience, we define the first two moments of the probability density over all possible clutch extensions: $n_b(t) = \int_{-\infty}^{\infty} P_b(x_c, t)dx_c$ and $\ell_b(t) = \int_{-\infty}^{\infty} x_c P_b(x_c,t)dx_c$, where n_b is the above-mentioned number of bound clutches and ℓ_b is the sum of clutch extensions. Governing equations for the first two moments can be obtained from quadrature of the conservation equation for the probability density function, yielding $\frac{dn_b}{dt} = k_{on}(n_c - n_b) - k_{off} \int_{-\infty}^{\infty} e^{\frac{\kappa_c|x_c|}{F_b}} P_b dx_c$, and $\frac{d\ell_b}{dt} = -k_{off} \int_{-\infty}^{\infty} x_c e^{\frac{\kappa_c|x_c|}{F_b}} P_b dx_c + v_e n_b$. A force balance on the substrate allows calculation of the traction force exerted on the substrate T as a function of the first-order moment of the probability density: $T = \kappa_s x_s = \kappa_c \ell_b$, where κ_s is the substrate stiffness constant and x_s is the substrate deformation. We take the time-derivative of the traction force to obtain an expression for the clutch elongation rate

$$v_e = \frac{1}{\kappa_s + n_b\kappa_c}\left[v_u\kappa_s\left(1 - \frac{\kappa_c\ell_b}{n_m F_m}\right) + \kappa_c k_{off} \int_{-\infty}^{\infty} x_c e^{\kappa_c|x_c|/F_b} P_b dx_c\right]. \quad (2)$$

TABLE 1 Dimensional Model Parameters

Symbol	Description	Estimated Values	Legend/References[a]
n_m+	number of myosin motors in the cellular protrusion	550	A
F_m+	single myosin motor stall force	0.6 – 2.3 pN	Chan and Odde (2); Molloy et al. (40); Ishijima et al. (41); Kishino and Yanagida (42); Tyska et al. (43)
v_u+	myosin unloaded velocity	120 – 240 nm·s^{-1}	Chan and Odde (2); Bangasser et al. (10); Bangasser and Odde (17); Stark et al. (44)
n_c*	number of clutches in the cellular protrusion	470	B
$k_{on}*$	clutch association rate constant	0.1 – 6 s^{-1}	Chan and Odde (2); Bangasser et al. (10); Bangasser and Odde (17); Litvinov et al. (45)
$k_{off}*$	unloaded clutch dissociation kinetic rate constant	0.1 – 6.5 s^{-1}	Chan and Odde (2); Bangasser et al. (10); Bangasser and Odde (17); Litvinov et al. (45); Le et al. (46)
F_b*	characteristic clutch-bond rupture force	1.7 pN	C
κ_c*	molecular clutch stiffness	[0.1 – 2] pN·nm^{-1}	D
$\theta*$	load-dependent clutch reinforcement strength	adjusted	–
$F_{th}*$	load-dependent clutch reinforcement threshold force	5 – 10 pN	Yao et al. (47); Yan et al. (48); Yu et al. (49); Yao et al. (50); Mekhdjian et al. (51)
$k_{off}^{catch}*$	unloaded clutch catch bond dissociation kinetic rate constant	adjusted	–
$F_b^{catch}*$	characteristic clutch catch bond rupture force	adjusted	–
$\kappa_s\#$	compliant substrate stiffness	[3.5 – 3.5 × 10^4] pN·μm^{-1}	E

[a]Parameter values are estimated in the supporting material. Motor parameters (plus symbol), clutch parameters (asterisk), cell environment parameters (hash symbol).

For convenience, we use dimensionless equations where we scale variables using k_{off}^{-1} as timescale, $n_m F_m/n_c\kappa_c$ as length scale, $n_m F_m k_{off}/n_c\kappa_c$ as velocity scale, and $n_c F_b$ as force scale: $t^* = tk_{off}$, $x^* = xn_c\kappa_c/n_m F_m$, $v_e^* = v_e n_c\kappa_c/n_m F_m k_{off}$, $P_b^* = P_b n_m F_m/n_c^2\kappa_c$, $T^* = T/n_c F_b$, where we have additionally normalized the probability density function by the total number of clutches n_c. The fraction of bound clutches is denoted as $n_b^* = n_b/n_c$. Henceforth, any variable accompanied by an asterisk is dimensionless. Nondimensionalization of the governing equations yields four dimensionless groups (Table 2): $F = n_m F_m/n_c F_b, \tau = k_{on}/k_{off}, \omega = v_u\kappa_c/F_b k_{off}, K = \kappa_s/n_c\kappa_c$. The myosin activity parameter F is the ratio of the total myosin stall force $n_m F_m$ over the characteristic maximum clutch elastic force $n_c F_b$. The clutch kinetic parameter τ is the ratio of the clutch association constant k_{on} over the clutch unloaded dissociation constant k_{off}. The parameter ω represents the ratio of the characteristic clutch unloaded dissociation time over the characteristic clutch loaded dissociation time. The parameter ω can also be described as the dimensionless myosin load-free velocity, or as the ratio of the characteristic elongation that a single clutch undergoes in the absence of cooperative clutch effects over the characteristic clutch rupture length. Notice that only large ω values are physiologically relevant ($\omega \gg 1$). Finally, the parameter K is the ratio of the substrate stiffness κ_s over the maximum effective clutch stiffness $n_c\kappa_c$. With these scalings, the conservation equation (1) and dimensionless clutch strain rate v_e^* read

$$\frac{\partial P_b^*}{\partial t^*} = \tau\left(1 - n_b^*\right)\delta^*\left(x_c^*\right) - e^{F|x_c^*|}P_b^* - v_e^*\frac{\partial P_b^*}{\partial x_c^*}, \quad (3)$$

$$v_e^* = \frac{1}{K + n_b^*}\left[\frac{\omega K}{F}\left(1 - \ell_b^*\right) + \int_{-\infty}^{\infty} x_c^* e^{F|x_c^*|}P_b^* dx_c^*\right] \quad (4)$$

where the first moment of the probability density over clutch extensions takes the form $\ell_b^* = \int_{-\infty}^{\infty} x_c^* P_b^* dx_c^*$. Notice that the traction force exerted on the compliant substrate is $T^* = F\ell_b^*$. Note, throughout the manuscript we use an overline symbol acting on a variable to denote the long time-averaged value of the variable.

RESULTS

Production of traction forces in individual cellular protrusions exhibit three different regimes

Cellular protrusions can generate traction forces and operate over three distinct regimes: a motor-dominated regime, a motor-clutch balanced regime, and a clutch-dominated regime. Previous analysis has focused only on the motor-clutch balanced regime (17). We have derived analytical expressions for the three key timescales that control traction force production: the characteristic time for available clutches to bind (i.e., mechanically couple actin filaments to the extracellular substrate) t_{bind}, the characteristic time for clutches to rupture due to force t_{rupt}, and the characteristic time for the substrate to reach its maximal deformation t_s^{max}. These three timescales depend on the different model parameters, dictate the cellular regime at which the protrusion operates, and are essential to understand traction force production and optimality conditions. We explored the high-dimensional parameter space by solving the governing equations of the mean-field model (Eqs. 3 and 4) using a finite-difference algorithm (see supporting material) and compared the numerical mean-field solution with the stochastic motor-clutch model version (2). We find a very good agreement between the mean-field solution and its stochastic counterpart for all the model parameters tested (Figs. 1,

TABLE 2 Dimensionless Model Parameters

Symbol	Definition	Description	Estimated Value[a]
F	$n_m F_m / n_c F_b$	myosin activity parameter	1.38
τ	k_{on}/k_{off}	clutch kinetic parameter	1
ω	$v_u \kappa_c / F_b k_{off}$	dimensionless myosin unloaded velocity	140
K	$\kappa_s / n_c \kappa_c$	dimensionless substrate stiffness	$\sim [10^{-5} - 10^{-1}]$
θ	θ	clutch reinforcement strength	adjusted
Δ	F_{th}/F_b	dimensionless clutch reinforcement threshold force	2.9
K_{off}	k_{off}^{catch}/k_{off}	dimensionless catch bond dissociation kinetic rate constant	adjusted
χ_b	F_b^{catch}/F_b	dimensionless clutch catch bond rupture force	adjusted
β_c	$\kappa_c \propto \beta_c$	clutch stiffness parameter	adjusted
ω'	ω/β_c	–	adjusted
K′	$K\beta_c$	–	adjusted

[a]Parameter values are estimated in the supporting material.

2, and 3). We explore the three different cellular regimes in detail below.

Clutch-dominated stalled regime

A distinct feature of the clutch-dominated regime, previously identified as the stalled regime (10,17), is that clutches dominate over motors. In this regime, the protrusion operates at its maximum efficiency by producing the maximum possible traction force, i.e., the total myosin stall force $\overline{T} = T_{max} = n_m F_m$ ($\overline{T}^* = F$ in dimensionless form), throughout a wide range of substrate stiffnesses (see Fig. 1 *B*, $F = 0.25$ and $F = 0.5$); hence, no single optimum substrate stiffness for maximum traction force exists. The clutch-dominated regime is therefore characterized by stiffness-independent traction forces as well as stiffness-independent clutch binding/unbinding kinetics, as shown in Fig. 2 by both the mean-field and stochastic motor-clutch model solutions of the time-averaged traction force (Fig. 2 *A*) and time-averaged fraction of bound clutches (Fig. 2 *B*, inset). The mean-field model captures the time-averaged traction force dynamics. In an unloaded protrusion, actin filaments flow rearward at the myosin load-free velocity. The first clutches that connect the fast-moving actin filaments with the deformable substrate undergo large extensions, since there is not enough elastic resistance against myosin pulling forces. This is shown in Fig. 2 *B* by the fat tail of the probability density function at short times. As time goes by, more clutches mechanically couple the actin cytoskeleton with the compliant substrate (Fig. 2 *B*, inset), which is manifested by the rise of the area under the probability density curve in Fig. 2 *B*, and elastic energy builds up in both substrate and bound clutches, slowing down actin retrograde flows. Low actin filament velocities lead clutches to dissociate stochastically before they can reach very large elongations, as demonstrated in Fig. 2 *B* by a reduction in the skewness of the probability distribution function at longer times (see green arrows in Fig. 2 *B*).

During loading, clutch binding dominates clutch unbinding in strong-clutch protrusions, there are enough bound clutches resisting myosin pulling forces at any instant in time, and the clutch complex never undergoes load-and-fail dynamics, as confirmed by Fig. 2 *A* and *B*. Clutch-dominated protrusions strain the substrate to its maximum deformation before clutch bonds break due to force ($t_s^{max} < t_{rupt}$); that is, F-actin retrograde flows vanish and the protrusion stalls. This inequality is satisfied (see derivation below) for protrusions with a motor activity parameter F lower than a threshold ($F < F_{c-i}^{crit}$). Here, F_{c-i}^{crit} is the critical motor activity parameter that sets the border between the clutch-dominated regime ($F < F_{c-i}^{crit}$) and the motor-clutch balanced regime ($F > F_{c-i}^{crit}$). Numerical values for F_{c-i}^{crit} are displayed in Fig. 2 *C* as a function of τ and ω for both soft and rigid substrates, and an analytical expression for the critical activity parameter F_{c-i}^{crit} has been estimated for soft substrates (see derivation below). The critical parameter F_{c-i}^{crit} monotonically increases as the parameter τ increases, as high-clutch-binding-rate protrusions require higher myosin forces to cause a clutch failure avalanche, an event that takes places when clutch bonds break in a runaway process giving rise to a failure of the entire clutch complex.

The dependence of F_{c-i}^{crit} on the dimensionless myosin load-free velocity ω is less straightforward. At the beginning of the loading cycle, stronger retrograde flows exist for larger values of ω. On very soft substrates, loading is slow, the initial strong retrograde flows largely deform the substrate, and clutches dissociate stochastically at long times. Therefore, clutch dynamics are not affected by the strength of actin filament retrograde flows and, accordingly, F_{c-i}^{crit} on soft substrates is nearly independent of ω, as shown in Fig. 2 *C*. On rigid substrates, on the other hand, clutches build up elastic energy very fast; thus, higher values of ω enhance clutch deformations at the onset of the loading cycle favoring load-and-fail dynamics over stall conditions. As a result, lower myosin forces are required for load-and-fail dynamics to occur on high-ω protrusions; that is, F_{c-i}^{crit}

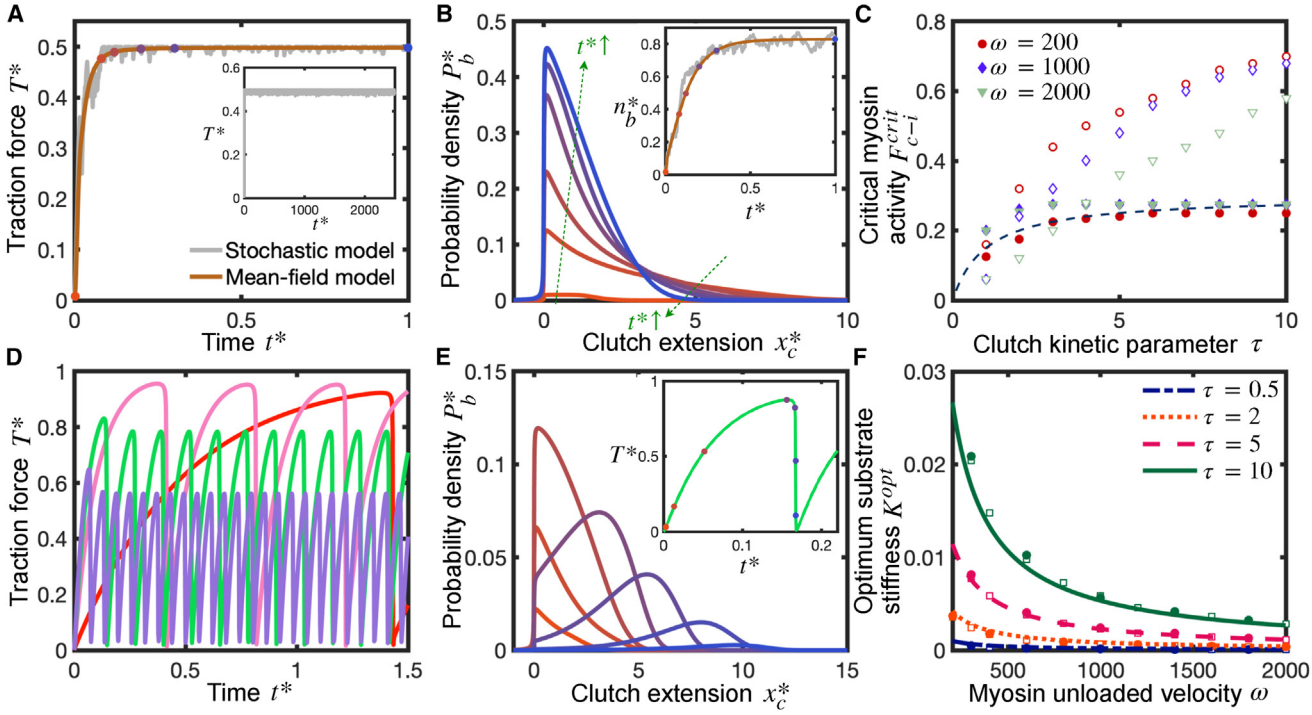

FIGURE 2 Clutch-dominated protrusions produce maximum possible traction forces and do not exhibit clutch failure avalanches, whereas cellular protrusions that operate in the intermediate regime features load-and-fail dynamics and produce maximum traction forces at an intermediate substrate stiffness. Temporal evolution of the dimensionless traction force (*A*), probability density function (*B*), and fraction of bound clutches (*B*, inset) in a clutch-dominated protrusion. The dimensionless probability density function is obtained by the mean-field model and sampled at the time points marked by symbols in (*A* and *B* inset). Color schemes of symbols in (*A* and *B* inset) and lines in (*B*) correspond to the same time points. In the clutch-dominated regime, long-time traction force and fraction of bound clutches approach the total myosin stall force $T = n_m F_m$ and unloaded equilibrium fraction of bound clutches $n_b = n_c k_{on}/(k_{on} + k_{off})$, respectively. Brown, mean-field model solution; gray, a single-trajectory of the stochastic model. (*A*, inset) Long-time stochastic single-trajectory. Parameter values: $F = 0.5, \tau = 10, \omega = 500, K = 1$. (*C*) Critical motor activity parameter F_{c-i}^{crit}, which sets the border between the clutch-dominated regime and the intermediate regime, as a function of the clutch kinetic parameter τ, for three values of the dimensionless myosin load-free velocity ω. Protrusions with $F < F_{c-i}^{crit}$ belong to the clutch-dominated regime and produce maximum available traction forces. Solid and open symbols correspond to the critical activity parameter in soft and rigid substrates, respectively. The dashed line is our analytical solution for soft substrates obtained via scaling analysis (Eq. 5). (*D*) Time evolution of dimensionless traction force for four different substrate stiffnesses: $K = 0.001$ (red), $K = 0.005$ (pink), $K = 0.008$ (green), and $K = 0.01$ (purple). Parameter values: $F = 1, \tau = 10, \omega = 2000$. (*E*) Temporal evolution of the dimensionless probability density function P_b^* and dimensionless traction force (inset). Symbols and color scheme in inset correspond to the time points where P_b^* is sampled. Parameter values: $F = 1, \tau = 10, \omega = 2000, K = 0.005$. (*F*) Dimensionless optimum substrate stiffness $K^{opt} = \kappa_s^{opt}/n_c\kappa_c$ as a function of the dimensionless myosin load-free velocity, ω, for four different values of the clutch kinetic parameter τ. The dimensionless clutch binding timescales as $t_{bind}^* \sim 1/(\tau + 1)$, whereas the dimensionless clutch rupture timescales as $t_{rupt}^* \sim (C_2/F + 1/K\omega)/(1 + 1/\tau)$. Solid lines correspond to our derived analytical solution (Eq. 6), open symbols correspond to the numerical solution of the mean-field model (Eqs. 3 and 4), and closed symbols correspond to the numerical solution of the stochastic model. Parameter value: $F = 2$. To see this figure in color, go online.

decreases with increasing ω on rigid substrates, as shown in Fig. 2 *C*.

Motor-clutch balanced regime

As its name suggests, the intermediate regime is a transitional regime between the free-flowing motor-dominated regime and the clutch-dominated stalled regime, where motors and clutches balance each other. The intermediate regime is characterized by load-and-fail dynamics (2) with stochastic transitions of slow and fast actin flows, also called stick-slip dynamics (34,36,53,54), and by the existence of a motor-sensitive optimum substrate stiffness for maximum traction force, as depicted in Fig. 1 *B* for $F \sim 1$. Cycles of loading and failure are illustrated in Figs. 2 *D* and S2 for different substrate stiffnesses. The mean frequency between two consecutive clutch cascading failure events decreases with substrate compliance, as shown in Fig. 2 *D*, and in agreement with Chan and Odde (2). At the beginning of loading, the elastic energy built up in the system is undertaken by the substrate/clutches on soft/stiff environments, respectively. Therefore, clutch lifetimes depend inversely on substrate rigidity, and higher frequency of clutch failures is observed on more rigid environments, as shown in Fig. S1 *B*. In the beginning of the loading cycle, the number of bound clutches is nearly independent of substrate stiffness, being mainly governed by clutch binding kinetics, as Fig. S2 *A* shows, where the four curves with different stiffnesses practically lie on top of each other at short times at the beginning of the first loading cycle. During this early

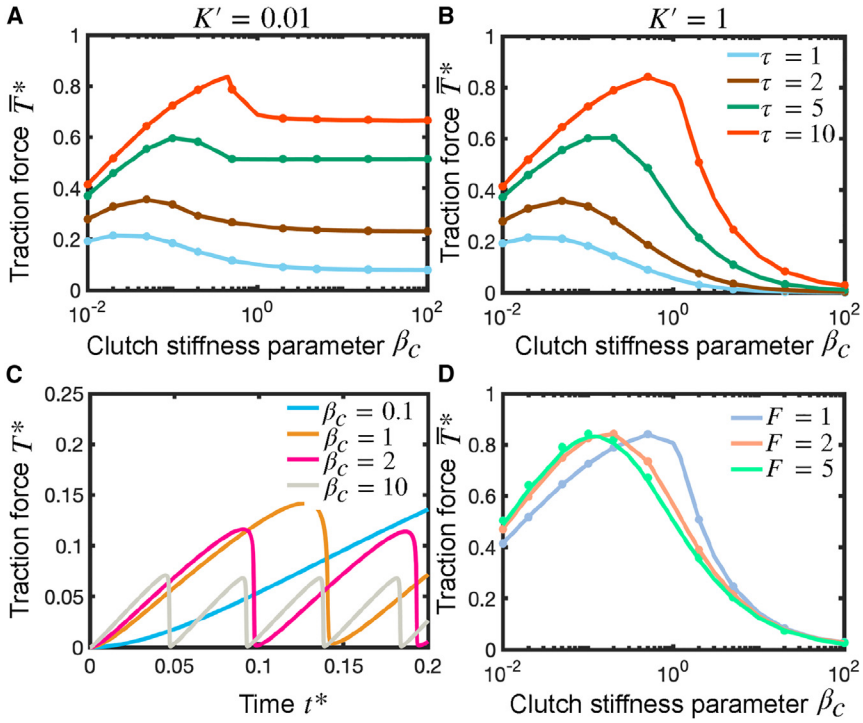

FIGURE 3 Traction force transmission is maximum at intermediate values of clutch stiffness. (*A* and *B*) Dimensionless time-averaged traction force $\overline{T}^*$ as a function of the clutch stiffness parameter β_c (notice that $\kappa_c \propto \beta_c$) for different values of the clutch kinetic parameter τ and for two values of the substrate stiffness parameter K' ($K = K'/\beta_c$): (*A*) $K' = 0.01$ and (*B*) $K' = 1$. Cellular traction forces on rigid substrates are very sensitive to clutch stiffness. The optimum clutch stiffness (optimum β_c) increases with the value of the clutch kinetic parameter. Parameter values: $F = 1$, $\omega' = 200$ ($\omega = \omega'\beta_c$). (*C*) Time evolution of traction force for four different values of the clutch stiffness parameter. Parameter values: $F = 1$, $\omega' = 200, K' = 0.01, \tau = 1$. (*D*) Dimensionless time-averaged traction force as a function of the effective clutch stiffness parameter for three different values of the myosin activity parameter F. Parameter values: $\omega' = 200$, $K' = 1$, $\tau = 10$. Solid lines correspond to the numerical solution of the mean-field model (Eqs. 3 and 4), and symbols correspond to the numerical solution of the stochastic motor-clutch model. To see this figure in color, go online.

phase, protrusions produce larger traction forces on more rigid substrates (Fig. 2 *D*). Later in the loading cycle, some clutches cannot sustain load any longer and eventually their clutch bonds break. The net clutch unbinding rate becomes greater than the clutch binding rate and the number of bound clutches begins to drop (Fig. S2 *A*), leading to an increase in clutch elongation rate (Fig. S2 *B*) and a reduction in substrate deformation rate (Fig. 2 *D*). As clutches gradually dissociate, the total load is redistributed among the remaining bound clutches, with an increase of load per clutch (Fig. 2 *E*). Eventually, the load cannot be sustained by the remaining clutches, and an instability occurs that eventuates in the rupture of all clutch bonds, a sudden fall in traction force (2), and the beginning of a new loading cycle. Notice that the duration of the clutch unbinding phase $(dn_b/dt < 0)$ is much longer than that of the clutch binding phase $(dn_b/dt > 0)$, especially on very soft substrates.

The boundary between the clutch-dominated stalled regime and the balanced regime is set by the condition $t_s^{max} \sim t_{rupt}$; that is, the time required to reach stall conditions matches the time needed for clutch bonds to break due to force. We perform scaling analysis (see supporting material) and find that, on soft substrates, the protrusion operates in the clutch-dominated regime when

$$F < F_{c-i}^{crit} = C_1 \frac{\tau}{\tau + 1}, \quad (5)$$

where $C_1 = 0.4$ is a constant that we estimate by fitting Eq. 5 with our numerical results. Fig. 2 *C* shows a very good agreement between our theoretical formula and numerical results.

Motor-dominated regime

Motor-dominated protrusions are characterized by a myosin-independent optimum stiffness, as shown in Fig. 1 *B*. Any changes in motor activity do not appreciably affect the dynamics of the protrusion (i.e., traction forces, clutch binding/unbinding kinetics, etc.). This is shown in Figs. 1 *B* and S1, where traction force, fraction of engaged clutches, and cycling time curves for $F = 10$, $F = 20$, and $F = 100$ lie on top of each other. Before any clutch links the actin cytoskeleton with the substrate, actin filaments flow rearward at the myosin load-free velocity. Once an individual clutch engages, it provides elastic resistance slowing down actin flows. In the high myosin limit, clutches are overpowered by motors and a further increase in motors does not alter actin flow speeds. Both clutch elongation and substrate elongation rates are myosin independent (see supporting material), which implies that motor-dominated protrusion dynamics are myosin insensitive. Motor-dominated protrusions also undergo load-and-fail dynamics and are still capable of sensing the rigidity of the environment. The previously identified free-flowing cellular state (10,17) is a particular case of the motor-dominated regime for motor-dominated protrusions on sufficiently rigid substrates, where traction forces build up at a fast rate, clutches reach a high tensional state very rapidly, and a state of frictional

slippage takes place where clutches continually dissociate by force before additional clutches can associate and share the load with the already bound clutches, limiting traction force production. We show that protrusions belong to the strong-motor regime when the condition $F \gg 0.05\tau$ is satisfied (see supporting material).

Optimum substrate stiffness for maximum traction force is reached when the clutch binding time equals the clutch rupture time

In this section, we apply scaling analysis to the mean-field model with the purpose of deriving an analytical expression for the optimum substrate stiffness (i.e., the substrate stiffness that maximizes traction forces). Previously, we found that optimum conditions for maximum traction force are reached when the time needed for available clutches to bind equals the cycle time (10,17). Here, we identify the cycle time as the characteristic time for clutches to rupture due to load; thus, we hypothesize that optimum conditions are reached when $t_{bind} \sim t_{rupt}$. We apply scaling analysis to estimate t_{bind} and t_{rupt} (see supporting material); we get:

$$\kappa_{s,i}^{opt} = C_2 \frac{n_c F_b k_{on}}{v_u} \frac{1}{1 - C_3 \frac{k_{on}}{k_{off}} \frac{n_c F_b}{n_m F_m}}. \quad (6)$$

where $C_2 = 0.4, C_3 = 0.05$. Figs. 2 *F* and S3 show that our theoretical expression is in very good agreement with our numerical results for all the motor-clutch dimensionless parameters. The optimum substrate stiffness in a protrusion that belongs to the intermediate regime, $\kappa_{s,i}^{opt}$, is myosin sensitive and independent of the effective clutch stiffness κ_c, as previously reported in other studies (10,17). Here, we explain this apparent counterintuitive result by realizing that both the characteristic clutch rupture length $\updownarrow_{rupt}$ and the characteristic clutch extension rate scale inversely to clutch stiffness. This implies that clutch rupture time is independent of clutch stiffness. Since neither the clutch binding rate nor the clutch rupture time depend on clutch stiffness, the substrate stiffness that maximizes traction forces does not depend on clutch stiffness, as Eq. 6 shows. We expect this result to hold for all physiologically relevant parameter values. In the non-physical situation where clutches dissociate stochastically instead of by force (small ω), the characteristic clutch rupture length would not be F_b/κ_c anymore, and optimum substrate stiffness would a priori depend on clutch stiffness. The optimum stiffness in motor-dominated protrusions reduces to $\kappa_{s,m}^{opt} = C_2 n_c F_b k_{on}/v_u$, where we have taken the limit $C_3 k_{on} n_c F_b / k_{off} n_m F_m \to 0$. We also find very good agreement between our theoretical prediction, the numerical solution of the mean-field model, and the solution of the dimensionless version of the stochastic motor-clutch model (2) for motor-dominated protrusions, as shown in Fig. S3, right. Our theoretical solution indicates that, in the high-motor regime, the optimum substrate stiffness is myosin insensitive, as depicted in Fig. 1 *B* ($F = 10, F = 20$). Overall, our results indicate that substrate stiffness optimality in motor-dominated protrusions can be shifted by tuning clutch activity but not motor activity, whereas optimality in motor-clutch balanced protrusions is sensitive to both myosin activity and clutches.

Traction force production is maximal at intermediate clutch stiffnesses

Since clutch stiffness is potentially a key mechanical property that the cell can control, and that can be engineered, e.g., via molecular tension sensors, we were interested in understanding the dependence of force transmission on clutch stiffness. In the previous section we showed that the optimum substrate stiffness κ_s^{opt} is insensitive to changes in clutch stiffness, κ_c. Force transmission, however, could a priori depend on clutch stiffness when the substrate stiffness differs from the optimum. To investigate this effect, we notice that among the four dimensionless parameters introduced, only two depend on κ_c: the parameter ω, which is proportional to κ_c, and the dimensionless substrate stiffness K, which depends inversely on κ_c. Accordingly, we introduce a new parameter, the clutch stiffness parameter β_c, such that $\omega = \omega'\beta_c$ and $K = K'/\beta_c$, where ω' and K' are, respectively, the values of the parameter ω and the dimensionless substrate stiffness K when $\beta_c = 1$. Consequently, by definition, increasing the value of the clutch stiffness parameter β_c is equivalent to proportionally increasing the effective clutch stiffness κ_c.

We investigated the dependence of the time-averaged force transmission on clutch stiffness by numerically solving our mean-field model equations. Our numerical results identified the existence of an optimum clutch stiffness for maximum traction force production (Fig. 3 *A* and *B*). Near-perfect agreement is found between the mean-field model solutions and the stochastic solutions. In the stiff-clutch limit, clutches provide enhanced elastic resistance to deformations, decreasing their strain rates. Their characteristic clutch rupture length, however, is inversely proportional to their stiffness (assuming that the clutch rupture force is constant). In the stiff-clutch limit, clutch lifetimes are low, especially on non-compliant substrates, and this is reflected in a low time-averaged number of bound clutches, as shown in Fig. S4. Even though the traction force buildup in stiff-clutch protrusions is extremely fast at the beginning of loading, the strong dependence of clutch lifetimes on their stiffness becomes the dominant effect and the resulting traction forces transmitted to the substrate are also low. In the soft-clutch limit, clutch extension rates are higher, but clutches disengage before high traction forces are produced, since the soft-clutch limit is associated with a slow buildup of traction forces, as shown

in Fig. 3 *C*. Consequently, there exists an optimum clutch stiffness that maximizes force transmission. Under the assumption that $v_u = 120\text{nm}\cdot\text{s}^{-1}$, $F_b = 2\text{pN}$, $k_{off} = 1\text{s}^{-1}$, and $\tau = 10\,(k_{on} = 10\text{s}^{-1})$, the mean-field model predicts that the optimum clutch stiffness is $\kappa_c^{opt} \approx 3.3\text{pN}\cdot\text{nm}^{-1}$, a clutch stiffness that is within the range of physiological clutch stiffness values.

Interestingly, the sensitivity of force transmission on clutch stiffness is significantly higher for protrusions on rigid substrates than for protrusions on soft substrates, as shown in Fig. 3 *A* and *B*. This can be explained by noticing that, on stiff substrates, the load-and-fail dynamics are largely governed by the mechanical properties of clutches. Consequently, the sensitivity of traction forces to changes in clutch stiffness is expected to be higher on this type of substrate. The optimum clutch stiffness increases for higher values of the clutch kinetic parameter τ, as shown by the shift in the optimum toward the right in Fig. 3 *A* and *B* and decreases with increasing values of the myosin activity parameter *F*, as shown in Fig. 3 *D*. Faster clutch recruitment or lower myosin activity strengthens clutches over motors, and stiffer clutches accelerate the buildup of traction forces, increasing the overall force transmission. This is consistent with Eqs. S51 and S52, where we show that the production of traction forces on rigid substrates in the limit of low myosin activity increases as the clutch stiffness increases. Direct comparison of Fig. 3 *A* and *B* indicates that the optimum clutch stiffness is barely sensitive to substrate compliance. Overall, these results show that there is an optimal clutch stiffness at which traction force is maximal.

Traction forces produced by protrusions on rigid substrates are maximal at intermediate myosin levels and unloaded myosin velocities

Although traditional traction force microscopy requires measurement of deformations in a compliant microenvironment (55–58), emerging molecular tension sensor technology is enabling measurement of traction forces on rigid substrates (59–61), significantly extending the range of potential traction force measurements to include stiff materials such as bone and medical devices. To characterize this rigid substrate regime in terms of optimal clutch stiffness, we investigated force transmission on rigid substrates and determined the time-averaged traction force $\overline{T}$, mean number of bound clutches $\overline{n}_b$ and mean clutch strain rate $\overline{v}_e$ (see supporting material for more details). We find very good agreement between our mean-field semi-analytical solutions and the solution from the stochastic model, as shown in Fig. 4. We find that traction forces on rigid environments exhibit a biphasic dependence on motor activity (Fig. 4, left), where the maximum time-averaged traction force is

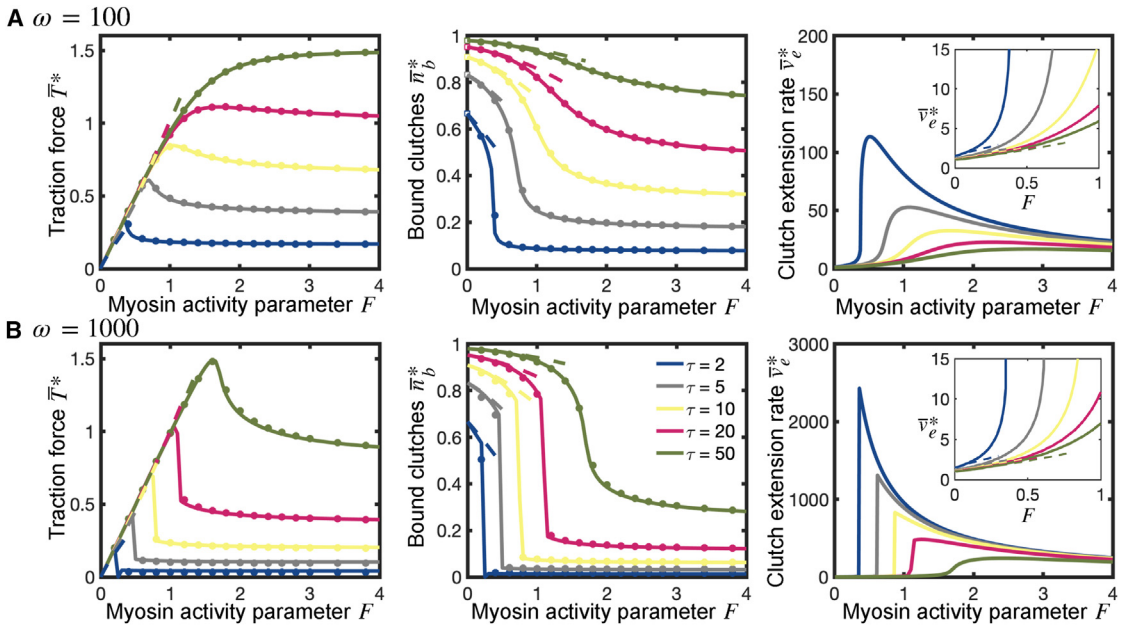

FIGURE 4 Force transmission on rigid substrates ($K \to \infty$) exhibits a biphasic dependence on motor activity. Time-averaged dimensionless traction force, fraction of bound clutches, and clutch strain rate as a function of the myosin activity parameter F for five different values of the clutch kinetic parameter τ, and two different values of the parameter ω ((*A*) First row, $\omega = 100$; (*B*) second row, $\omega = 1000$). Traction force and fraction of bound clutches monotonically increase with τ, whereas clutch strain rate decreases with τ. Traction force exhibits a maximum at an intermediate value of the myosin activity parameter F^{opt} (see Fig. 5 *A* for further analysis). Clutch extension rate also exhibits a maximum at an intermediate value of the myosin activity parameter $F > F^{opt}$. Curves reach F-independent asymptotic values at high myosin activity (large F) (see Fig. 5 *B* and *C* for additional details). Solid lines correspond to the numerical solution of the mean-field model (Eqs. S31–S36) and symbols correspond to the numerical solution of the stochastic model. Dashed lines correspond to our low-F asymptotic solutions (Eqs. S51, S46, and S49). To see this figure in color, go online.

reached at an intermediate value of the myosin activity parameter F^{opt}, which monotonically decreases with τ and ω (Fig. 5 *A*). The time-averaged clutch extension rate also exhibits a maximum at a value of F that is greater than F^{opt} (Fig. 4, right).

We additionally use perturbation theory to derive analytical expressions for the time-averaged clutch elongation rate, number of bound clutches, and traction force by low-motor ($F\to 0$) and high-motor ($F\to\infty$) activity protrusions (see supporting material for additional details). The derived analytical expressions for low-motor protrusions and high-motor protrusions agree very well with our numerical solutions, as shown in Figs. 4 and 5, respectively. Interestingly, the $\overline{T}^*(\tau,\omega)$ high-motor curves reach a maximum value at an optimum value ω^{opt}, as shown in Fig. 5 *B*. This optimum dimensionless load-free velocity exhibits a nearly linear dependence with τ, as shown in the inset of Fig. 5 *B*. In dimensional form, it implies that an intermediate value of $\kappa_c v_u/F_b k_{off}$ exists that maximizes traction forces, and it scales linearly with the ratio k_{on}/k_{off}. Thus, our model can help guide molecular tension sensor design and prediction of traction forces on rigid surfaces such as bone and implantable medical devices.

Load-dependent clutch reinforcement increases the optimum substrate stiffness and optimum clutch stiffness

So far, we have assumed that clutches behave as slip bonds. However, since many cell types exhibit adhesion reinforcement, we added load-dependent clutch adhesion reinforcement on force transmission into our analysis (14,28,51,62–64). We assumed that the effective clutch association rate linearly depends on the actual fraction of clutches that are bound and whose load exceeds the clutch reinforcement threshold force F_{th} (51). The conservation equation for the probability density thus reads:

$$\frac{\partial P_b^*}{\partial t^*} = \tau\left(1+\theta\int_{\Delta/F}^{\infty} P_b^* dx_c^*\right)\left(1-n_b^*\right)\delta^*\left(x_c^*\right) - e^{F\left|x_c^*\right|}P_b^* - v_e^*\frac{\partial P_b^*}{\partial x_c^*}, \tag{7}$$

where we have introduced a clutch reinforcement strength parameter θ and dimensionless clutch reinforcement threshold force $\Delta = F_{th}/F_b$, so that $\Delta>>1$ favors bond rupture under load and $\Delta<<1$ favors reinforcement over rupture. We numerically solved Eq. 7 and found that, in protrusions with a small unloaded myosin velocity parameter ω and low number of myosin motors over clutches, i.e., low F, clutch reinforcement prevents frictional slippage on rigid substrates and force transmission increases monotonically with substrate stiffness, as shown in Fig. 6 *A*. By contrast, motor-dominated protrusions, i.e., high F, are associated with large clutch force loading rates due to large myosin pulling forces and require an anomalously high clutch reinforcement parameter to strengthen clutches, prevent frictional slippage, and allow the production of substantial traction forces on rigid substrates, as manifested by the low traction force transmitted on rigid substrates (Figs. 6 *B* and S6 *D*). For larger values of the unloaded myosin velocity parameter, ω (i.e., $\omega = 2000$ instead of 200), the traction vs. substrate stiffness curves are monotonically increasing for sufficiently high values of the clutch reinforcement strength parameter θ, whereas they display a biphasic behavior for low values of θ, as shown in Fig. S5 *A*. Force transmission on rigid substrates monotonically decreases with an increase in the characteristic clutch reinforcement force Δ, and it can be strongly influenced by

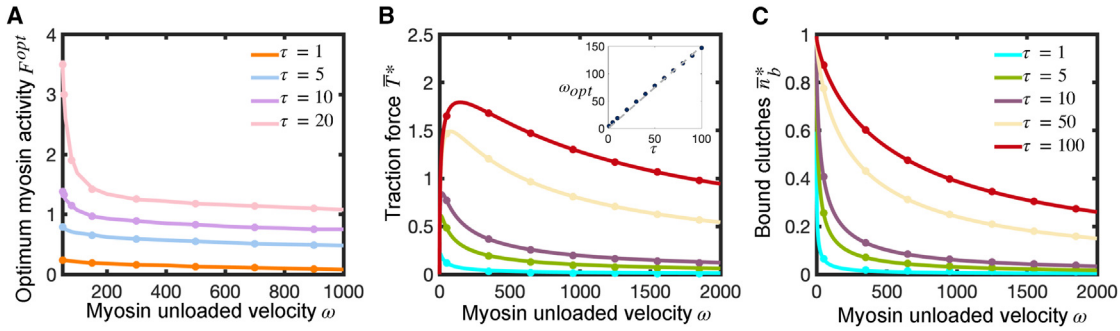

FIGURE 5 Traction force produced by a strong-motor protrusion on rigid substrates reaches a maximum at an intermediate value of the myosin load-free velocity parameter ω. (*A*) Optimum myosin activity parameter for maximum traction force on rigid substrates as a function of ω for four different values of the clutch kinetic parameter τ. The optimum activity F^{opt} monotonically decreases with τ and ω. (*B* and *C*) Dimensionless time-averaged traction force (*B*) and average fraction of bound clutches (*C*) for a strong-motor protrusion ($F\to\infty$) on rigid substrates ($K\to\infty$), as a function of ω for five different values of τ. Force transmission shows a biphasic dependence on the parameter ω, with an optimum ω^{opt} that increases linearly with τ (see inset in (*B*)). Number of bound clutches increases monotonically with τ and ω. Solid lines correspond to the analytical solutions of the mean-field model (Eqs. S55 and S57), and symbols are the solutions of the stochastic model. Near-perfect agreement is found between analytical and stochastic solutions. To see this figure in color, go online.

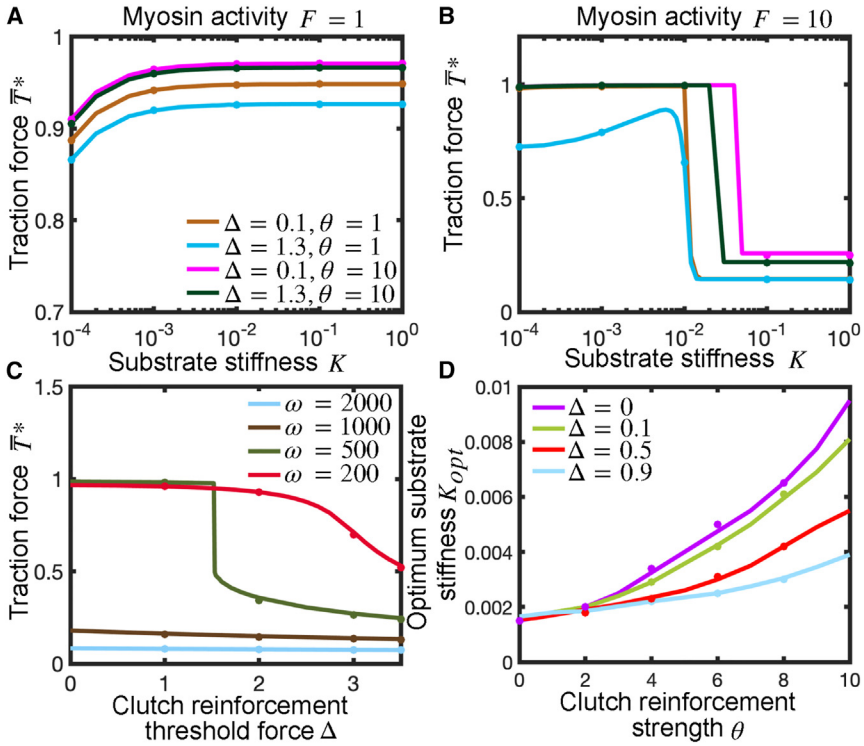

FIGURE 6 Influence of clutch reinforcement on traction force and optimal substrate stiffness. Force transmission on rigid substrates results from a competition between load-dependent clutch reinforcement and myosin-mediated clutch loading rates. (*A* and *B*) Dimensionless time-averaged traction force as a function of substrate stiffness for different values of the clutch reinforcement parameter θ and clutch reinforcement threshold force Δ. Parameter values: $\tau = 1$, $\omega = 200$, (A) $F = 1$ and (*B*) $F = 10$. (*C*) Dimensionless time-averaged traction force on rigid substrates ($K \to \infty$) as a function of Δ for four different values of the unloaded velocity parameter ω. Parameter values: $\theta = 10, F = 1, \tau = 5$. (*D*) Optimum substrate stiffness as a function of θ for different values of Δ. Parameter values: $\omega = 200, F = 1, \tau = 1$. Solid lines are the numerical solution of the developed mean-field model (Eq. 7), and symbols are the numerical solutions of the stochastic motor-clutch model. To see this figure in color, go online.

the value of Δ, particularly for sufficiently high θ values and low enough ω values, as shown in Figs. 6 *C* and S5 *B*. Clutch reinforcement shifts the optimum substrate stiffness for maximal force production to stiffer substrates, as shown in Figs. 6 *D* and S5 *D*, and this optimum stiffness shift is significant only for low values of the unloaded myosin velocity parameter ω, as Fig. S5 *C* shows. Our mean-field model with clutch reinforcement also shows that adhesion reinforcement on rigid substrates shifts the optimum unloaded velocity parameter to larger values and the optimum clutch stiffness to higher stiffnesses, as depicted in Fig. S6 (parts B and C, respectively). Finally, we investigated the role of clutch catch bond behavior on force transmission, modeled as described in the supplement, and find nearly independent traction force generation on catch properties as shown in Fig. S7). Altogether, the inclusion of load-dependent clutch-bond reinforcement increases the optimal substrate stiffness and optimal clutch stiffness, but inclusion of clutch catch bonds has relatively little effect on optimal substrate stiffness.

DISCUSSION

In the present study, we developed a generalized mean-field motor-clutch model that provides new insights of force transmission of adhesion-based cellular protrusions on compliant elastic substrates and provides a quantitative analysis of regulation of force transmission by modulation of cellular components and extracellular rigidity. Unlike prior studies, the developed model explores motor-clutch imbalanced regimes, investigates novel traction optimality conditions, studies load-dependent reinforcement and catch bond behaviors, and quantifies traction force sensitivity to all the model parameters through the identification of key dimensionless parameters. Our model results indicate that shifting substrate stiffness optimality in cells that operate in the motor-dominated regime can be achieved by tuning clutch activity, whereas changes in motor activity will not produce any substrate mechanical optimality alterations. Motor-clutch balanced protrusions, on the other hand, are characterized by an optimum substrate stiffness sensitive to both myosin activity and clutches, whereas clutch-dominated stalled protrusions are characterized by substrate stiffness-insensitive traction forces, as previously shown (10). Our theoretical results additionally give the necessary and sufficient conditions required for the cell to operate at each regime. Determining the traction force production regime at which cells operate in physiological conditions would be a major step toward identifying the key cell molecular candidates and/or stromal components to target with the aim of controlling cell traction force production and substrate stiffness optimality and, in turn, cell adhesion-based migration (11,12).

We additionally found that traction force generation away from optimality is strongly influenced by clutch stiffness, especially on rigid substrates, and discovered the existence of an intermediate clutch stiffness for maximum force transmission. Our results strongly suggest that cells containing

very soft or very stiff clutches will have reduced cell migration capabilities, especially on rigid substrates. Suboptimal cell migration conditions in the soft-clutch and stiff-clutch limits are caused by a slow buildup of traction forces and by frequent frictional slippage behavior, respectively. These results could be important for understanding cell behavior on stiff materials such as tissue culture plastic or glass, implanted biomedical devices, and bone. Furthermore, the biphasic dependence of traction force generation on clutch stiffness predicted here is reminiscent of the reported biphasic cell migration dependence on clutch component expression levels in an ex vivo disease model (11), and it could have important implications in the development of therapeutic strategies to treat cancer. One possible plan of action could involve molecular engineering by inserting deformable domains between two molecular clutch components with the aim of arresting cancer cell migration, in a similar fashion to the insertion of molecular tension sensors with controlled stiffness in focal adhesion complexes (65). Optimization of the mechanical properties of these domains would require cell-specific parameterization of the different model parameters, including the development of new techniques to accurately measure the effective clutch complex stiffness and the identification of the softest clutch bonds that largely contribute to the effective clutch complex softening. Although the stiffness of some clutch components has been estimated in multiple studies (47,66,67), clutch stiffness data are scarce (68) (Table 1). Our clutch stiffness results also suggest that the insertion of molecular tension sensors to measure cellular traction forces might alter traction force generation for sufficiently soft tension sensors delivering inaccurate traction force measurements. A specific example of such molecular tension sensors is digital readout sensors based on disruption of DNA duplexes with high force ($>$20 pN) thresholds (69–71). Consequently, accurate traction force measurements via molecular tension sensors require the design and engineering of stiff sensors, much stiffer than molecular clutches. Molecular tension sensors typically rely on a tension sensor module that is composed of two fluorophores connected by a force-sensitive linker peptide that extends reversibly in response to mechanical forces. The ideal fabrication strategy would be to design the force-sensitive linker peptide to be as stiff as possible to enhance measurement accuracy without penalizing sensor sensitivity and range. Our work also provides a physical explanation for why the optimum substrate stiffness for maximal force transmission is independent of clutch stiffness (10,17), since clutch rupture times are independent of clutch stiffness near the optimum. Our findings also show that motor-dominated protrusions shift the clutch stiffness optimum toward softer clutch rigidities, whereas clutch-dominated protrusions shift it toward stiffer clutch rigidities. Our work potentially suggests that clutch stiffness could play an important role not only in cell migration speed but also in changes in cell polarization direction by modulating clutch association and dissociation kinetics and/or actin retrograde flow strengths and, in turn, protein transport (72).

In addition, we found that protrusions on rigid substrates display a biphasic dependence of force transmission on motor activity. This is particularly interesting since motor activity levels can be modulated by the internal cellular state as well as by environmental cellular conditions (73,74). Our model predicts that a significant increase in motor activity can dramatically diminish adhesion-based traction forces and potentially suppress adhesion-based cell motility. Consequently, cells might require alternative mechanisms to efficiently migrate within highly confined spaces or within other mechanochemical environments that promote high-motor activity levels. Our mean-field model also predicts that traction force produced by a strong-motor protrusion on rigid substrates reaches a maximum at an intermediate value of the myosin load-free velocity parameter. This novel result could have important implications in understanding the contribution of different myosin motor types on force transmission, as different myosin motors produce distinct force-velocity curves and have different myosin load-free velocities (75–77). It would also be interesting to test this prediction experimentally, and it encourages the design of motor-oriented therapeutic strategies to modulate traction force production and potentially migration of cells that operate in a high-motor activity cellular state. The reported biphasic dependence of force transmission on motor activity and unloaded motor velocity could be potentially tested via novel molecular tension sensor experiments and opens new research avenues in biological systems with stiff cellular environments. Unraveling the mechanics of cellular force production and migration in stiff cellular environments is crucial in many aspects of health and human physiology. Cell migration dysregulation in stiff environments is associated with many processes in development and human diseases, such as clinical complications, tissue remodeling and immune modulation in inflammatory responses near implanted medical devices (78,79), bone cancer metastasis (80), fibrosis in cancer (81,82), calcified bone remodeling processes and homeostasis (83), and dental lamina development and degradation processes (84). The high stiffness regime is also important for understanding cell interactions with rigid implantable biomedical devices.

Our findings also predict that load-dependent clutch reinforcement can substantially increase the traction force produced by protrusions that display load-and-fail dynamics, and it can significantly shift the optimum substrate and clutch stiffnesses to larger values. Although traction force-substrate stiffness curves were found to be monotonically increasing functions in reinforced protrusions with small unloaded myosin velocities and relatively low number of myosin motors over clutches, motor-dominated protrusions displayed a biphasic dependence of force transmission on

substrate stiffness for the clutch reinforcement strengths explored, requiring anomalously high clutch reinforcement strengths to prevent frictional slippage and to allow the production of significant traction forces on rigid substrates. These results provide key insights to effectively design novel cell and stromal engineering strategies to strengthen or weaken clutch reinforcement with the aim of, respectively, enhancing or decreasing traction force production and potentially cell migration capabilities.

Our current study has some limitations. We have addressed cycles of extension and retraction of single-cell protrusions and adhesion dynamics at the cell edge and did not study either cell polarization or cell migration. Existing biophysical models in compliant (12) and non-compliant (53,54) substrates and experimental work (72,85–92) have captured spontaneous symmetry breaking and a great diversity of cell migration patterns, including persistent migration and bipedal locomotion, that emerge from fluctuations in cellular components that spatially modulate force generation and resisting forces. Our developed mean-field model can be further extended to elucidate biophysical mechanisms underlying differential coordinated actin dynamics and traction force generation among cellular protrusions that cause cell symmetry breaking/polarization and to better understand 2D and 3D adhesion-based cell migration capabilities on compliant cellular microenvironments. We have assumed that the mechanical properties of clutches are those of the weakest link in the adhesion complex, a standard assumption in the motor-clutch framework. The constitutive adhesion proteins that form clutch complexes flow retrogradely at different speeds (93,94), with actin-binding proteins flowing at high speeds and more coherently, matrix-binding proteins flowing at low speeds and mostly incoherently, and core clutch proteins linking actin-binding and matrix-binding proteins flowing at intermediate speeds and with somewhat coherent motion. The reported differences in retrograde flow speeds agree well with the motor-clutch hypothesis, and this could imply the absence of a clear "weakest link" and that the constitutive protein-protein adhesion bonds may have similar mechanical properties with multiple bonds influencing force transmission. The reported differential coherence could suggest that adhesion complex links undergo slippage and do not maintain robust connections (59), which could limit force transmission and efficiency. We have also assumed that the substrate is a Hookean elastic material. However, tissues and extracellular fibril networks are not linearly elastic but display complex mechanical behaviors, including nonlinear elasticity such as stress stiffening and stress softening (95,96), mechanical plasticity (97), and viscoelasticity (98,99). Force loading rates are very slow in soft substrates and viscous dissipation provides additional resistance to retrograde myosin pulling forces, which increases the initial force loading rate (37,100), reducing actin retrograde flows, and increasing membrane front speeds and cell migration, consistent with enhanced experimental and computational cell migration speeds reported on soft substrates with faster stress relaxation times (100). The mechanical response of the extracellular space to cellular forces plays a critical role in force transmission and cell migration, and determining the constitutive mechanical model that better describes the extracellular space is a potential opportunity for future experimental and theoretical studies. In addition, our model does not account for spatial density gradients of myosin motors, molecular clutches, and actin filaments. Low traction stresses produced by epithelial cells were measured at the leading edge (lamellipodium) and cell body, whereas traction stresses peaked in the region between the lamellipodium base and the cell body where focal adhesions maturate (101,102). F-actin speeds reached a maximum at the leading edge and inversely correlated with distance from the cell edge. Traction forces and F-actin flows were therefore found to be inversely related in the lamellipodium and focal adhesion region, consistent with the motor-clutch framework. Focal adhesion disassembly and reduced myosin activity in the lamella or cell body region (103) can explain the drastic drop in traction stresses and F-actin speeds in those areas further away from the leading edge. Finally, additional studies are needed to identify the main adhesion clutch constituents, as well as the key mechanisms for efficient cellular force transmission/migration and activation of mechanotransduction pathways in different complex mechanochemical microenvironments. The mechanotransduction of cellular forces transmitted to the extracellular fibril network into biochemical signals leads to transcriptional regulation in the nucleus (104–106) that can modulate force transmission, thus influencing cell migration in non-trivial ways. Further understanding will speed up the discovery of new therapeutic strategies to treat human disease for improved patient outcomes.

SUPPORTING MATERIAL

Supporting material can be found online at https://doi.org/10.1016/j.bpj.2023.07.012.

AUTHOR CONTRIBUTIONS

R.A.M. designed research, developed the biophysical model, performed mathematical derivations and numerical simulations, and wrote the manuscript. P.P.P and D.J.O. secured funding, oversaw all aspects of the study, and provided edits to the manuscript.

ACKNOWLEDGMENTS

Research reported in this publication was supported by NIH grants U54CA210190, P01CA254849, and U54CA268069. We thank members of the Provenzano and Odde labs for helpful conversations throughout the course of this work. The content of this work is solely the responsibility

of the authors and does not necessarily represent the official views of the NIH.

DECLARATION OF INTERESTS

P.P.P. is a member of the Scientific Advisory Board for Parthenon Therapeutics.

REFERENCES

1. Giannone, G., B. J. Dubin-Thaler, …, M. P. Sheetz. 2004. Periodic lamellipodial contractions correlate with rearward actin waves. *Cell.* 116:431–443. https://doi.org/10.1016/s0092-8674(04)00058-3. https://www.ncbi.nlm.nih.gov/pubmed/15016377.
2. Chan, C. E., and D. J. Odde. 2008. Traction dynamics of filopodia on compliant substrates. *Science.* 322:1687–1691. https://doi.org/10.1126/science.1163595. https://www.ncbi.nlm.nih.gov/pubmed/19074349.
3. Mitchison, T., and M. Kirschner. 1988. Cytoskeletal dynamics and nerve growth. *Neuron.* 1:761–772. https://doi.org/10.1016/0896-6273(88)90124-9. https://www.ncbi.nlm.nih.gov/pubmed/3078414.
4. Lauffenburger, D. A., and A. Wells. 2001. Getting a grip: new insights for cell adhesion and traction. *Nat. Cell Biol.* 3:E110–E112. https://doi.org/10.1038/35074631. https://www.ncbi.nlm.nih.gov/pubmed/11331893.
5. Balaban, N. Q., U. S. Schwarz, …, B. Geiger. 2001. Force and focal adhesion assembly: a close relationship studied using elastic micropatterned substrates. *Nat. Cell Biol.* 3:466–472. https://doi.org/10.1038/35074532. https://www.ncbi.nlm.nih.gov/pubmed/11331874.
6. Bershadsky, A. D., N. Q. Balaban, and B. Geiger. 2003. Adhesion-dependent cell mechanosensitivity. *Annu. Rev. Cell Dev. Biol.* 19:677–695. https://doi.org/10.1146/annurev.cellbio.19.111301.153011. https://www.ncbi.nlm.nih.gov/pubmed/14570586.
7. Lin, C. H., and P. Forscher. 1995. Growth cone advance is inversely proportional to retrograde F-actin flow. *Neuron.* 14:763–771. https://doi.org/10.1016/0896-6273(95)90220-1. https://www.ncbi.nlm.nih.gov/pubmed/7536426.
8. Watanabe, N., and T. J. Mitchison. 2002. Single-molecule speckle analysis of actin filament turnover in lamellipodia. *Science.* 295:1083–1086. https://doi.org/10.1126/science.1067470. https://www.ncbi.nlm.nih.gov/pubmed/11834838.
9. Lin, C. H., E. M. Espreafico, …, P. Forscher. 1996. Myosin drives retrograde F-actin flow in neuronal growth cones. *Neuron.* 16:769–782. https://doi.org/10.1016/s0896-6273(00)80097-5. https://www.ncbi.nlm.nih.gov/pubmed/8607995.
10. Bangasser, B. L., S. S. Rosenfeld, and D. J. Odde. 2013. Determinants of maximal force transmission in a motor-clutch model of cell traction in a compliant microenvironment. *Biophys. J.* 105:581–592. https://doi.org/10.1016/j.bpj.2013.06.027. https://www.ncbi.nlm.nih.gov/pubmed/23931306.
11. Klank, R. L., S. A. Decker Grunke, …, D. J. Odde. 2017. Biphasic Dependence of Glioma Survival and Cell Migration on CD44 Expression Level. *Cell Rep.* 18:23–31. https://doi.org/10.1016/j.celrep.2016.12.024. https://www.ncbi.nlm.nih.gov/pubmed/28052252.
12. Bangasser, B. L., G. A. Shamsan, …, D. J. Odde. 2017. Shifting the optimal stiffness for cell migration. *Nat. Commun.* 8, 15313. https://doi.org/10.1038/ncomms15313. https://www.ncbi.nlm.nih.gov/pubmed/28530245.
13. Elosegui-Artola, A., E. Bazellières, …, P. Roca-Cusachs. 2014. Rigidity sensing and adaptation through regulation of integrin types. *Nat. Mater.* 13:631–637. https://doi.org/10.1038/nmat3960. https://www.ncbi.nlm.nih.gov/pubmed/24793358.
14. Elosegui-Artola, A., R. Oria, …, P. Roca-Cusachs. 2016. Mechanical regulation of a molecular clutch defines force transmission and transduction in response to matrix rigidity. *Nat. Cell Biol.* 18:540–548. https://doi.org/10.1038/ncb3336. https://www.ncbi.nlm.nih.gov/pubmed/27065098.
15. Ray, A., O. Lee, …, P. P. Provenzano. 2017. Anisotropic forces from spatially constrained focal adhesions mediate contact guidance directed cell migration. *Nat. Commun.* 8, 14923. https://doi.org/10.1038/ncomms14923. https://www.ncbi.nlm.nih.gov/pubmed/28401884.
16. Lauffenburger, D. A., and A. F. Horwitz. 1996. Cell migration: a physically integrated molecular process. *Cell.* 84:359–369. https://doi.org/10.1016/s0092-8674(00)81280-5. https://www.ncbi.nlm.nih.gov/pubmed/8608589.
17. Bangasser, B. L., and D. J. Odde. 2013. Master equation-based analysis of a motor-clutch model for cell traction force. *Cell. Mol. Bioeng.* 6:449–459. https://doi.org/10.1007/s12195-013-0296-5. https://www.ncbi.nlm.nih.gov/pubmed/24465279.
18. Mitrossilis, D., J. Fouchard, …, A. Asnacios. 2009. Single-cell response to stiffness exhibits muscle-like behavior. *Proc. Natl. Acad. Sci. USA.* 106:18243–18248. https://doi.org/10.1073/pnas.0903994106. https://www.ncbi.nlm.nih.gov/pubmed/19805036.
19. DiMilla, P. A., K. Barbee, and D. A. Lauffenburger. 1991. Mathematical model for the effects of adhesion and mechanics on cell migration speed. *Biophys. J.* 60:15–37. https://doi.org/10.1016/S0006-3495(91)82027-6. https://www.ncbi.nlm.nih.gov/pubmed/1883934.
20. Palecek, S. P., J. C. Loftus, …, A. F. Horwitz. 1997. Integrin-ligand binding properties govern cell migration speed through cell-substratum adhesiveness. *Nature.* 385:537–540. https://doi.org/10.1038/385537a0. https://www.ncbi.nlm.nih.gov/pubmed/9020360.
21. Huttenlocher, A., M. H. Ginsberg, and A. F. Horwitz. 1996. Modulation of cell migration by integrin-mediated cytoskeletal linkages and ligand-binding affinity. *J. Cell Biol.* 134:1551–1562. https://doi.org/10.1083/jcb.134.6.1551. https://www.ncbi.nlm.nih.gov/pubmed/8830782.
22. Khatiwala, C. B., S. R. Peyton, and A. J. Putnam. 2006. Intrinsic mechanical properties of the extracellular matrix affect the behavior of pre-osteoblastic MC3T3-E1 cells. *Am. J. Physiol. Cell Physiol.* 290:C1640–C1650. https://doi.org/10.1152/ajpcell.00455.2005. https://www.ncbi.nlm.nih.gov/pubmed/16407416.
23. Peyton, S. R., and A. J. Putnam. 2005. Extracellular matrix rigidity governs smooth muscle cell motility in a biphasic fashion. *J. Cell. Physiol.* 204:198–209. https://doi.org/10.1002/jcp.20274. https://www.ncbi.nlm.nih.gov/pubmed/15669099.
24. Stroka, K. M., and H. Aranda-Espinoza. 2009. Neutrophils display biphasic relationship between migration and substrate stiffness. *Cell Motil Cytoskeleton.* 66:328–341. https://doi.org/10.1002/cm.20363. https://www.ncbi.nlm.nih.gov/pubmed/19373775.
25. Tan, J., H. Shen, and W. M. Saltzman. 2001. Micron-scale positioning of features influences the rate of polymorphonuclear leukocyte migration. *Biophys. J.* 81:2569–2579. https://doi.org/10.1016/S0006-3495(01)75901-2. https://www.ncbi.nlm.nih.gov/pubmed/11606271.
26. Lang, N. R., K. Skodzek, …, B. Fabry. 2015. Biphasic response of cell invasion to matrix stiffness in three-dimensional biopolymer networks. *Acta Biomater.* 13:61–67. https://doi.org/10.1016/j.actbio.2014.11.003. https://www.ncbi.nlm.nih.gov/pubmed/25462839.
27. Zaman, M. H., L. M. Trapani, …, P. Matsudaira. 2006. Migration of tumor cells in 3D matrices is governed by matrix stiffness along with cell-matrix adhesion and proteolysis. *Proc. Natl. Acad. Sci. USA.* 103:10889–10894. https://doi.org/10.1073/pnas.0604460103. https://www.ncbi.nlm.nih.gov/pubmed/16832052.
28. Elosegui-Artola, A., X. Trepat, and P. Roca-Cusachs. 2018. Control of Mechanotransduction by Molecular Clutch Dynamics. *Trends Cell Biol.* 28:356–367. https://doi.org/10.1016/j.tcb.2018.01.008. https://www.ncbi.nlm.nih.gov/pubmed/29496292.
29. Lo, C. M., H. B. Wang, …, Y. L. Wang. 2000. Cell movement is guided by the rigidity of the substrate. *Biophys. J.* 79:144–152. https://doi.org/10.1016/S0006-3495(00)76279-5. https://www.ncbi.nlm.nih.gov/pubmed/10866943.
30. Califano, J. P., and C. A. Reinhart-King. 2010. Substrate Stiffness and Cell Area Predict Cellular Traction Stresses in Single Cells and Cells in

Contact. *Cell. Mol. Bioeng.* 3:68–75. https://doi.org/10.1007/s12195-010-0102-6. https://www.ncbi.nlm.nih.gov/pubmed/21116436.

31. Ambrosi, D., A. Duperray, …, C. Verdier. 2009. Traction patterns of tumor cells. *J. Math. Biol.* 58:163–181. https://doi.org/10.1007/s00285-008-0167-1. https://www.ncbi.nlm.nih.gov/pubmed/18392826.

32. Guvendiren, M., and J. A. Burdick. 2012. Stiffening hydrogels to probe short- and long-term cellular responses to dynamic mechanics. *Nat. Commun.* 3:792. https://doi.org/10.1038/ncomms1792. https://www.ncbi.nlm.nih.gov/pubmed/22531177.

33. Bressloff, P. C. 2020. Stochastic resetting and the mean-field dynamics of focal adhesions. *Phys. Rev. E.* 102, 022134. https://doi.org/10.1103/PhysRevE.102.022134. https://www.ncbi.nlm.nih.gov/pubmed/32942383.

34. Sabass, B., and U. S. Schwarz. 2010. Modeling cytoskeletal flow over adhesion sites: competition between stochastic bond dynamics and intracellular relaxation. *J. Phys. Condens. Matter.* 22, 194112. https://doi.org/10.1088/0953-8984/22/19/194112. https://www.ncbi.nlm.nih.gov/pubmed/21386438.

35. Li, Y., P. Bhimalapuram, and A. R. Dinner. 2010. Model for how retrograde actin flow regulates adhesion traction stresses. *J. Phys. Condens. Matter.* 22, 194113. https://doi.org/10.1088/0953-8984/22/19/194113. https://www.ncbi.nlm.nih.gov/pubmed/21386439.

36. Sens, P. 2013. Rigidity sensing by stochastic sliding friction. *Europhys. Lett.* 104:38003.

37. Gong, Z., S. E. Szczesny, …, V. B. Shenoy. 2018. Matching material and cellular timescales maximizes cell spreading on viscoelastic substrates. *Proc. Natl. Acad. Sci. USA.* 115:E2686–E2695. https://doi.org/10.1073/pnas.1716620115. https://www.ncbi.nlm.nih.gov/pubmed/29507238.

38. Huang, D. L., N. A. Bax, …, A. R. Dunn. 2017. Vinculin forms a directionally asymmetric catch bond with F-actin. *Science.* 357:703–706. https://doi.org/10.1126/science.aan2556. https://www.ncbi.nlm.nih.gov/pubmed/28818948.

39. Strohmeyer, N., M. Bharadwaj, …, D. J. Müller. 2017. Fibronectin-bound α5β1 integrins sense load and signal to reinforce adhesion in less than a second. *Nat. Mater.* 16:1262–1270. https://doi.org/10.1038/nmat5023. https://www.ncbi.nlm.nih.gov/pubmed/29115292.

40. Molloy, J. E., J. E. Burns, …, D. C. White. 1995. Movement and force produced by a single myosin head. *Nature.* 378:209–212. https://doi.org/10.1038/378209a0. https://www.ncbi.nlm.nih.gov/pubmed/7477328.

41. Ishijima, A., H. Kojima, …, T. Yanagida. 1996. Multiple- and single-molecule analysis of the actomyosin motor by nanometer-piconewton manipulation with a microneedle: unitary steps and forces. *Biophys. J.* 70:383–400. https://doi.org/10.1016/S0006-3495(96)79582-6. https://www.ncbi.nlm.nih.gov/pubmed/8770215.

42. Kishino, A., and T. Yanagida. 1988. Force measurements by micromanipulation of a single actin filament by glass needles. *Nature.* 334:74–76. https://doi.org/10.1038/334074a0. https://www.ncbi.nlm.nih.gov/pubmed/3386748.

43. Tyska, M. J., D. E. Dupuis, …, S. Lowey. 1999. Two heads of myosin are better than one for generating force and motion. *Proc. Natl. Acad. Sci. USA.* 96:4402–4407. https://doi.org/10.1073/pnas.96.8.4402. https://www.ncbi.nlm.nih.gov/pubmed/10200274.

44. Stark, B. C., T. E. Sladewski, …, M. Lord. 2010. Tropomyosin and myosin-II cellular levels promote actomyosin ring assembly in fission yeast. *Mol. Biol. Cell.* 21:989–1000. https://doi.org/10.1091/mbc.e09-10-0852. https://www.ncbi.nlm.nih.gov/pubmed/20110347.

45. Litvinov, R. I., A. Mekler, …, J. W. Weisel. 2012. Resolving two-dimensional kinetics of the integrin αIIbβ3-fibrinogen interactions using binding-unbinding correlation spectroscopy. *J. Biol. Chem.* 287:35275–35285. https://doi.org/10.1074/jbc.M112.404848. https://www.ncbi.nlm.nih.gov/pubmed/22893701.

46. Le, S., M. Yu, and J. Yan. 2019. Direct single-molecule quantification reveals unexpectedly high mechanical stability of vinculin-talin/α-catenin linkages. *Sci. Adv.* 5, eaav2720. https://doi.org/10.1126/sciadv.aav2720. https://www.ncbi.nlm.nih.gov/pubmed/31897422.

47. Yao, M., B. T. Goult, …, J. Yan. 2016. The mechanical response of talin. *Nat. Commun.* 7, 11966. https://doi.org/10.1038/ncomms11966. https://www.ncbi.nlm.nih.gov/pubmed/27384267.

48. Yan, J., M. Yao, …, M. P. Sheetz. 2015. Talin Dependent Mechanosensitivity of Cell Focal Adhesions. *Cell. Mol. Bioeng.* 8:151–159. https://doi.org/10.1007/s12195-014-0364-5. https://www.ncbi.nlm.nih.gov/pubmed/26097520.

49. Yu, M., S. Le, …, J. Yan. 2019. Force-Dependent Regulation of Talin-KANK1 Complex at Focal Adhesions. *Nano Lett.* 19:5982–5990. https://doi.org/10.1021/acs.nanolett.9b01732. https://www.ncbi.nlm.nih.gov/pubmed/31389241.

50. Yao, M., B. T. Goult, …, J. Yan. 2014. Mechanical activation of vinculin binding to talin locks talin in an unfolded conformation. *Sci. Rep.* 4:4610. https://doi.org/10.1038/srep04610. https://www.ncbi.nlm.nih.gov/pubmed/24714394.

51. Mekhdjian, A. H., F. Kai, …, V. M. Weaver. 2017. Integrin-mediated traction force enhances paxillin molecular associations and adhesion dynamics that increase the invasiveness of tumor cells into a three-dimensional extracellular matrix. *Mol. Biol. Cell.* 28:1467–1488. https://doi.org/10.1091/mbc.E16-09-0654. https://www.ncbi.nlm.nih.gov/pubmed/28381423.

52. Bell, G. I. 1978. Models for the specific adhesion of cells to cells. *Science.* 200:618–627. https://doi.org/10.1126/science.347575. https://www.ncbi.nlm.nih.gov/pubmed/347575.

53. Ron, J. E., P. Monzo, …, N. S. Gov. 2020. One-dimensional cell motility patterns. *Phys. Rev. Res.* 2, 033237.

54. Sens, P. 2020. Stick-slip model for actin-driven cell protrusions, cell polarization, and crawling. *Proc. Natl. Acad. Sci. USA.* 117:24670–24678. https://doi.org/10.1073/pnas.2011785117. https://www.ncbi.nlm.nih.gov/pubmed/32958682.

55. Dembo, M., and Y. L. Wang. 1999. Stresses at the cell-to-substrate interface during locomotion of fibroblasts. *Biophys. J.* 76:2307–2316. https://doi.org/10.1016/S0006-3495(99)77386-8. https://www.ncbi.nlm.nih.gov/pubmed/10096925.

56. Munevar, S., Y. Wang, and M. Dembo. 2001. Traction force microscopy of migrating normal and H-ras transformed 3T3 fibroblasts. *Biophys. J.* 80:1744–1757. https://doi.org/10.1016/s0006-3495(01)76145-0. https://www.ncbi.nlm.nih.gov/pubmed/11259288.

57. Plotnikov, S. V., B. Sabass, …, C. M. Waterman. 2014. High-resolution traction force microscopy. *Methods Cell Biol.* 123:367–394. https://doi.org/10.1016/B978-0-12-420138-5.00020-3. https://www.ncbi.nlm.nih.gov/pubmed/24974038.

58. Butler, J. P., I. M. Tolić-Nørrelykke, …, J. J. Fredberg. 2002. Traction fields, moments, and strain energy that cells exert on their surroundings. *Am. J. Physiol. Cell Physiol.* 282:C595–C605. https://doi.org/10.1152/ajpcell.00270.2001. https://www.ncbi.nlm.nih.gov/pubmed/11832345.

59. Tan, S. J., A. C. Chang, …, A. R. Dunn. 2020. Regulation and dynamics of force transmission at individual cell-matrix adhesion bonds. *Sci. Adv.* 6, eaax0317. https://doi.org/10.1126/sciadv.aax0317. https://www.ncbi.nlm.nih.gov/pubmed/32440534.

60. Grashoff, C., B. D. Hoffman, …, M. A. Schwartz. 2010. Measuring mechanical tension across vinculin reveals regulation of focal adhesion dynamics. *Nature.* 466:263–266. https://doi.org/10.1038/nature09198. https://www.ncbi.nlm.nih.gov/pubmed/20613844.

61. Fischer, L. S., S. Rangarajan, …, C. Grashoff. 2021. Molecular Force Measurement with Tension Sensors. *Annu. Rev. Biophys.* 50:595–616. https://doi.org/10.1146/annurev-biophys-101920-064756. https://www.ncbi.nlm.nih.gov/pubmed/33710908.

62. Swaminathan, V., and C. M. Waterman. 2016. The molecular clutch model for mechanotransduction evolves. *Nat. Cell Biol.* 18:459–461. https://doi.org/10.1038/ncb3350. https://www.ncbi.nlm.nih.gov/pubmed/27117328.

63. Isomursu, A., K. Y. Park, …, D. J. Odde. 2022. Directed cell migration towards softer environments. *Nat. Mater.* 21:1081–1090. https://doi.org/10.1038/s41563-022-01294-2. https://www.ncbi.nlm.nih.gov/pubmed/35817964.

64. Shamsan, G. A., and D. J. Odde. 2019. Emerging technologies in mechanotransduction research. *Curr. Opin. Chem. Biol.* 53:125–130. https://doi.org/10.1016/j.cbpa.2019.08.002. https://www.ncbi.nlm.nih.gov/pubmed/31618703.

65. LaCroix, A. S., A. D. Lynch, …, B. D. Hoffman. 2018. Tunable molecular tension sensors reveal extension-based control of vinculin loading. *Elife*. 7, e33927. https://doi.org/10.7554/eLife.33927. https://www.ncbi.nlm.nih.gov/pubmed/30024378.

66. del Rio, A., R. Perez-Jimenez, …, M. P. Sheetz. 2009. Stretching single talin rod molecules activates vinculin binding. *Science*. 323:638–641. https://doi.org/10.1126/science.1162912. https://www.ncbi.nlm.nih.gov/pubmed/19179532.

67. Chen, Y., H. Lee, …, C. Zhu. 2017. Force regulated conformational change of integrin α. *Matrix Biol.* 60–61:70–85. https://doi.org/10.1016/j.matbio.2016.07.002. https://www.ncbi.nlm.nih.gov/pubmed/27423389.

68. Nakao, N., K. Maki, …, T. Adachi. 2019. Talin is required to increase stiffness of focal molecular complex in its early formation process. *Biochem. Biophys. Res. Commun.* 518:579–583. https://doi.org/10.1016/j.bbrc.2019.08.091. https://www.ncbi.nlm.nih.gov/pubmed/31451222.

69. Pawlak, M. R., A. T. Smiley, …, W. R. Gordon. 2023. RAD-TGTs: high-throughput measurement of cellular mechanotype via rupture and delivery of DNA tension probes. *Nat. Commun.* 14:2468. https://doi.org/10.1038/s41467-023-38157-6. https://www.ncbi.nlm.nih.gov/pubmed/37117218.

70. Brockman, J. M., H. Su, …, K. Salaita. 2020. Live-cell super-resolved PAINT imaging of piconewton cellular traction forces. *Nat. Methods.* 17:1018–1024. https://doi.org/10.1038/s41592-020-0929-2. https://www.ncbi.nlm.nih.gov/pubmed/32929270.

71. Jo, M. H., W. T. Cottle, and T. Ha. 2019. Real-Time Measurement of Molecular Tension during Cell Adhesion and Migration Using Multiplexed Differential Analysis of Tension Gauge Tethers. *ACS Biomater. Sci. Eng.* 5:3856–3863. https://doi.org/10.1021/acsbiomaterials.8b01216. https://www.ncbi.nlm.nih.gov/pubmed/33438425.

72. Maiuri, P., J. F. Rupprecht, …, R. Voituriez. 2015. Actin flows mediate a universal coupling between cell speed and cell persistence. *Cell.* 161:374–386. https://doi.org/10.1016/j.cell.2015.01.056. https://www.ncbi.nlm.nih.gov/pubmed/25799384.

73. Lomakin, A. J., C. J. Cattin, …, M. Piel. 2020. The nucleus acts as a ruler tailoring cell responses to spatial constraints. *Science.* 370, eaba2894. https://doi.org/10.1126/science.aba2894. https://www.ncbi.nlm.nih.gov/pubmed/33060332.

74. Venturini, V., F. Pezzano, …, V. Ruprecht. 2020. The nucleus measures shape changes for cellular proprioception to control dynamic cell behavior. *Science.* 370, eaba2644. https://doi.org/10.1126/science.aba2644. https://www.ncbi.nlm.nih.gov/pubmed/33060331.

75. Bottinelli, R., M. Canepari, …, C. Reggiani. 1996. Force-velocity properties of human skeletal muscle fibres: myosin heavy chain isoform and temperature dependence. *J. Physiol.* 495:573–586. https://doi.org/10.1113/jphysiol.1996.sp021617. https://www.ncbi.nlm.nih.gov/pubmed/8887767.

76. Weiss, S., R. Rossi, …, M. A. Geeves. 2001. Differing ADP release rates from myosin heavy chain isoforms define the shortening velocity of skeletal muscle fibers. *J. Biol. Chem.* 276:45902–45908. https://doi.org/10.1074/jbc.M107434200. https://www.ncbi.nlm.nih.gov/pubmed/11590173.

77. Reggiani, C., R. Bottinelli, and G. J. M. Stienen. 2000. Sarcomeric Myosin Isoforms: Fine Tuning of a Molecular Motor. *News Physiol. Sci.* 15:26–33. https://doi.org/10.1152/physiologyonline.2000.15.1.26. https://www.ncbi.nlm.nih.gov/pubmed/11390872.

78. Noskovicova, N., B. Hinz, and P. Pakshir. 2021. Implant Fibrosis and the Underappreciated Role of Myofibroblasts in the Foreign Body Reaction. *Cells.* 10, 1794. https://doi.org/10.3390/cells10071794. https://www.ncbi.nlm.nih.gov/pubmed/34359963.

79. Su, P., Y. Tian, …, A. Qian. 2018. Mesenchymal Stem Cell Migration during Bone Formation and Bone Diseases Therapy. *Int. J. Mol. Sci.* 19, 2343. https://doi.org/10.3390/ijms19082343. https://www.ncbi.nlm.nih.gov/pubmed/30096908.

80. Jones, D. H., T. Nakashima, …, J. M. Penninger. 2006. Regulation of cancer cell migration and bone metastasis by RANKL. *Nature.* 440:692–696. https://doi.org/10.1038/nature04524. https://www.ncbi.nlm.nih.gov/pubmed/16572175.

81. Boulter, L., E. Bullock, …, V. G. Brunton. 2021. The fibrotic and immune microenvironments as targetable drivers of metastasis. *Br. J. Cancer.* 124:27–36. https://doi.org/10.1038/s41416-020-01172-1. https://www.ncbi.nlm.nih.gov/pubmed/33239677.

82. Piersma, B., M. K. Hayward, and V. M. Weaver. 2020. Fibrosis and cancer: A strained relationship. *Biochim. Biophys. Acta Rev. Canc.* 1873, 188356. https://doi.org/10.1016/j.bbcan.2020.188356. https://www.ncbi.nlm.nih.gov/pubmed/32147542.

83. Florencio-Silva, R., G. R. d. S. Sasso, …, P. S. Cerri. 2015. Biology of Bone Tissue: Structure, Function, and Factors That Influence Bone Cells. *BioMed Res. Int.* 2015, 421746. https://doi.org/10.1155/2015/421746. https://www.ncbi.nlm.nih.gov/pubmed/26247020.

84. Buchtová, M., J. Stembírek, …, A. S. Tucker. 2012. Early regression of the dental lamina underlies the development of diphyodont dentitions. *J. Dent. Res.* 91:491–498. https://doi.org/10.1177/0022034512442896. https://www.ncbi.nlm.nih.gov/pubmed/22442052.

85. Guetta-Terrier, C., P. Monzo, …, N. C. Gauthier. 2015. Protrusive waves guide 3D cell migration along nanofibers. *J. Cell Biol.* 211:683–701. https://doi.org/10.1083/jcb.201501106. https://www.ncbi.nlm.nih.gov/pubmed/26553933.

86. Prahl, L. S., M. R. Stanslaski, …, D. J. Odde. 2020. Predicting Confined 1D Cell Migration from Parameters Calibrated to a 2D Motor-Clutch Model. *Biophys. J.* 118:1709–1720. https://doi.org/10.1016/j.bpj.2020.01.048. https://www.ncbi.nlm.nih.gov/pubmed/32145191.

87. Barnhart, E., K. C. Lee, …, A. Mogilner. 2015. Balance between cell-substrate adhesion and myosin contraction determines the frequency of motility initiation in fish keratocytes. *Proc. Natl. Acad. Sci. USA.* 112:5045–5050. https://doi.org/10.1073/pnas.1417257112. https://www.ncbi.nlm.nih.gov/pubmed/25848042.

88. Barnhart, E. L., G. M. Allen, …, J. A. Theriot. 2010. Bipedal locomotion in crawling cells. *Biophys. J.* 98:933–942. https://doi.org/10.1016/j.bpj.2009.10.058. https://www.ncbi.nlm.nih.gov/pubmed/20303850.

89. Dembo, M., T. Oliver, …, K. Jacobson. 1996. Imaging the traction stresses exerted by locomoting cells with the elastic substratum method. *Biophys. J.* 70:2008–2022. https://doi.org/10.1016/S0006-3495(96)79767-9. https://www.ncbi.nlm.nih.gov/pubmed/8785360.

90. Lee, J., M. Leonard, …, K. Jacobson. 1994. Traction forces generated by locomoting keratocytes. *J. Cell Biol.* 127:1957–1964. https://doi.org/10.1083/jcb.127.6.1957. https://www.ncbi.nlm.nih.gov/pubmed/7806573.

91. Balzer, E. M., Z. Tong, …, K. Konstantopoulos. 2012. Physical confinement alters tumor cell adhesion and migration phenotypes. *Faseb. J.* 26:4045–4056. https://doi.org/10.1096/fj.12-211441. https://www.ncbi.nlm.nih.gov/pubmed/22707566.

92. García, J. R., and A. J. García. 2014. Cellular mechanotransduction: sensing rigidity. *Nat. Mater.* 13:539–540. https://doi.org/10.1038/nmat3996. https://www.ncbi.nlm.nih.gov/pubmed/24845988.

93. Hu, K., L. Ji, …, C. M. Waterman-Storer. 2007. Differential transmission of actin motion within focal adhesions. *Science.* 315:111–115. https://doi.org/10.1126/science.1135085. https://www.ncbi.nlm.nih.gov/pubmed/17204653.

94. Owen, L. M., A. S. Adhikari, …, A. R. Dunn. 2017. A cytoskeletal clutch mediates cellular force transmission in a soft, three-dimensional extracellular matrix. *Mol. Biol. Cell.* 28:1959–1974. https://doi.org/10.1091/mbc.E17-02-0102. https://www.ncbi.nlm.nih.gov/pubmed/28592635.

95. Licup, A. J., S. Münster, …, F. C. MacKintosh. 2015. Stress controls the mechanics of collagen networks. *Proc. Natl. Acad. Sci. USA.* 112:9573–9578. https://doi.org/10.1073/pnas.1504258112. https://www.ncbi.nlm.nih.gov/pubmed/26195769.

96. Han, Y. L., P. Ronceray, …, M. Guo. 2018. Cell contraction induces long-ranged stress stiffening in the extracellular matrix. *Proc. Natl. Acad. Sci. USA.* 115:4075–4080. https://doi.org/10.1073/pnas.1722619115. https://www.ncbi.nlm.nih.gov/pubmed/29618614.

97. Kim, J., J. Feng, …, B. Sun. 2017. Stress-induced plasticity of dynamic collagen networks. *Nat. Commun.* 8:842. https://doi.org/10.1038/s41467-017-01011-7. https://www.ncbi.nlm.nih.gov/pubmed/29018207.

98. Chaudhuri, O., L. Gu, …, D. J. Mooney. 2016. Hydrogels with tunable stress relaxation regulate stem cell fate and activity. *Nat. Mater.* 15:326–334. https://doi.org/10.1038/nmat4489. https://www.ncbi.nlm.nih.gov/pubmed/26618884.

99. Chaudhuri, O. 2017. Viscoelastic hydrogels for 3D cell culture. *Biomater. Sci.* 5:1480–1490. https://doi.org/10.1039/c7bm00261k. https://www.ncbi.nlm.nih.gov/pubmed/28584885.

100. Adebowale, K., Z. Gong, …, O. Chaudhuri. 2021. Enhanced substrate stress relaxation promotes filopodia-mediated cell migration. *Nat. Mater.* 20:1290–1299. https://doi.org/10.1038/s41563-021-00981-w. https://www.ncbi.nlm.nih.gov/pubmed/33875851.

101. Gardel, M. L., B. Sabass, …, C. M. Waterman. 2008. Traction stress in focal adhesions correlates biphasically with actin retrograde flow speed. *J. Cell Biol.* 183:999–1005. https://doi.org/10.1083/jcb.200810060. https://www.ncbi.nlm.nih.gov/pubmed/19075110.

102. Craig, E. M., J. Stricker, …, A. Mogilner. 2015. Model for adhesion clutch explains biphasic relationship between actin flow and traction at the cell leading edge. *Phys. Biol.* 12, 035002. https://doi.org/10.1088/1478-3975/12/3/035002. https://www.ncbi.nlm.nih.gov/pubmed/25969948.

103. Broussard, J. A., D. J. Webb, and I. Kaverina. 2008. Asymmetric focal adhesion disassembly in motile cells. *Curr. Opin. Cell Biol.* 20:85–90. https://doi.org/10.1016/j.ceb.2007.10.009. https://www.ncbi.nlm.nih.gov/pubmed/18083360.

104. Sakabe, M., J. Fan, …, M. Xin. 2017. YAP/TAZ-CDC42 signaling regulates vascular tip cell migration. *Proc. Natl. Acad. Sci. USA.* 114:10918–10923. https://doi.org/10.1073/pnas.1704030114. https://www.ncbi.nlm.nih.gov/pubmed/28973878.

105. Dupont, S., L. Morsut, …, S. Piccolo. 2011. Role of YAP/TAZ in mechanotransduction. *Nature.* 474:179–183. https://doi.org/10.1038/nature10137. https://www.ncbi.nlm.nih.gov/pubmed/21654799.

106. Dupont, S. 2016. Role of YAP/TAZ in cell-matrix adhesion-mediated signalling and mechanotransduction. *Exp. Cell Res.* 343:42–53. https://doi.org/10.1016/j.yexcr.2015.10.034. https://www.ncbi.nlm.nih.gov/pubmed/26524510.

Biophysical Journal, Volume *122*

Supplemental information

Optimal cell traction forces in a generalized motor-clutch model

Roberto Alonso-Matilla, Paolo P. Provenzano, and David J. Odde

Optimal cell traction forces in a generalized motor-clutch model

Roberto Alonso-Matilla[1-3], Paolo P. Provenzano[1-6] and David J. Odde[1-4]

[1]Department of Biomedical Engineering, University of Minnesota, Minneapolis, MN, USA
[2] University of Minnesota Physical Sciences in Oncology Center, Minneapolis, MN, USA
[3] University of Minnesota Center for Multiparametric Imaging of Tumor Immune Microenvironments, Minneapolis, MN, USA
[4] Masonic Cancer Center, University of Minnesota, USA
[5] Department of Hematology, Oncology, and Transplantation, University of Minnesota, USA
[6] Stem Cell Institute, University of Minnesota, USA

SUPPLEMENTAL INFORMATION

Estimation of model parameters

We proceed to estimate the different motor-clutch model parameters shown in Tables 1 and 2 (Main Text).

Table 1

A. We estimate the total number of myosin motors in the cellular protrusion by assuming that the cellular protrusion contains a similar motor surface density as that of the cytokinetic ring. At the onset of constriction, the well-characterized fission yeast contractile ring contains $\rho_{myo}^{ring} \sim 3.6 \times 10^3$ myosin-II polypeptides/μm^2 (1). Assuming that the protrusion geometry can be approximated as a cylinder of length $\ell_{prot} \sim 1\ \mu m$ and diameter $d_{prot} \sim 50\ nm$, the estimated number of motors in the protrusion is $n_m \sim 550$. Notice that motor activity levels can be modulated by the internal state of the cell as well as by environmental cellular conditions.

B. The surface density of adhesion molecules reported is $\rho_c \sim 3.1 \times 10^3\ units/\mu m^2$ (2). The number of clutches can be approximated as (see legend A): $n_c \sim \rho_c/(\ell_{prot} d_{prot} \pi) \sim 470$. Elosegui-Artola et al. reported similar integrin densities on the membrane $\rho_c \sim [500 - 2500]\ units/\mu m^2$ (3). Alternatively, one could estimate the cell-specific number of clutches available in the protrusion by fitting experimentally measured traction forces and actin retrograde flow speeds with model predictions.

C. Direct single molecule quantification assays revealed a talin-vinculin clutch bond rupture force of $F_b = k_B T/\Delta = 4.114\ \mathrm{pN \cdot nm}/2.4\ \mathrm{nm} \sim 1.7\mathrm{pN}$, where Δ is the clutch transition distance that was estimated by fitting the force-dependent clutch rupture rate using Bell's model. The work by Jiang et al. suggest that clutch bond rupture forces are of the same order of magnitude: $F_b \sim 2\mathrm{pN}$ (4).

D. The stiffnesses of some clutch components such as talin (5)**,** the molecular complex formed between $\alpha_v\beta_3$ and $FN_{III7-10}$ (6), and a talin-vinculin tandem (7), have been estimated in multiple studies, with reported values within the range $\kappa_c \sim [0.2 - 2]\ \mathrm{pN \cdot nm^{-1}}$. Proteomic studies have identified hundreds of molecules associated with focal adhesions (8). Therefore, the effective clutch stiffness cannot just be reduced to single clutch-component stiffness values. The effective clutch stiffness has been estimated as the slope at low extensions of force-extension curves from AFM measurements by approaching the cell with an AFM coated probe, establishing contact with the cell surface and then pulling the probe away from the cell surface (9). Although in these experiments cell-probe mechanical interactions might be mediated by a single molecular clutch, it will be important in future studies to decouple clutch and whole-cell mechanical resistance to AFM pulling forces. Although existing data suggest that clutch effective stiffness lies within the $\mathrm{pN/nm}$ range, there is a need to better estimate effective clutch complex stiffnesses, characterize nonlinear mechanical clutch stiffness characteristics and identify the softest bonds within the molecular clutch complex that largely contribute to the effective clutch complex softening.

E. The motor-clutch framework models the substrate as a one-dimensional linear spring. Assuming that the substrate behaves as a semi-infinite incompressible elastic material and that focal adhesions are far from each other, we can estimate the effective substrate stiffness κ_s from the equivalent substrate Young's modulus E_s as $\kappa_s = 2\pi d_s E_s/9$ (10,11), where d_s is the focal adhesion diameter. With a typical focal adhesion diameter of $d_s \sim 500\ \mathrm{nm}$ and a reasonable range of substrate Young's modulus $E_s = [0.01 - 100]\ \mathrm{kPa}$, we get $\kappa_s = [3.5 - 3.5 \times 10^4]\ \mathrm{pN \cdot \mu m^{-1}}$. The

equivalence substrate stiffness-substrate Young's modulus has also been studied for different focal adhesion sizes and force distributions (12).

Table 2

We have used the following dimensional parameter values to estimate the dimensionless motor-clutch parameters: $n_m = 550$, $F_m = 2\ \mathrm{pN}$, $v_u = 240\ \mathrm{nm \cdot s^{-1}}$, $n_c = 470$, $k_{on} = 1\ \mathrm{s^{-1}}$, $k_{off} = 1\ \mathrm{s^{-1}}$, $F_b = 1.7\ \mathrm{pN}$, $\kappa_c = 1\ \mathrm{pN \cdot nm^{-1}}$, $\kappa_s = [3.5 - 3.5 \times 10^4]\ \mathrm{pN \cdot \mu m^{-1}}$, $F_{th} = 5\ \mathrm{pN}$. Using the estimated values on Table S2, the developed model predicts traction forces within the range $[59 - 145]\ \mathrm{pN}$, with a maximum traction force for a substrate Young's modulus of $2.7\ \mathrm{kPa}$. Cell-specific data should be used to parameterize the model and accurately predict generated traction forces, actin retrograde flows and the regime at which the cell operates.

Mean-field conservation equation of the probability density

The Markovian nature of clutch dynamics allow us to relate the probability density P_b at time $t + \Delta t$ to its value at an earlier time t with an integral equation of the form

$$P_b(x_c, t + \Delta t) = k_{on}(n_c - n_b)\delta(x_c)\Delta t - k_{off}^{load} P_b(x_c, t)\Delta t + \int_{-\infty}^{\infty} d(\Delta x_c)\, P_b(x_c - \Delta x_c, t)\phi(x_c - \Delta x_c | \Delta x_c, \Delta t). \quad (S1)$$

The first term on the RHS of Eq. (S1) corresponds to clutch binding kinetics, where the Dirac delta function $\delta(x_c)$ has been included to specify that the clutch length at the binding time is equal to its resting length. The second term on the RHS of Eq. (S1) accounts for clutch unbinding kinetics, where the clutch lifetime decreases exponentially by force according to Bell's law $k_{off}^{load} = k_{off}\, e^{\kappa_c |x_c| / F_b}$. The third term on the RHS of Eq. (S1) accounts for clutch extensions, where $\phi(x_c | \Delta x_c, \Delta t)$ is the probability of clutches with extension x_c undergoing an extension Δx_c during a time Δt. Ignoring the binding/unbinding kinetic terms, Eq. (S1) says that the probability density

of clutches to be with extension x_c at time $t + \Delta t$ is given by the product of the probability density for clutches to be with extension $x_c - \Delta x_c$ at time t, multiplied by the probability of experiencing an extension Δx_c during a period of time Δt, and integrated over all possible extensions. Notice that the probability of experiencing a clutch extension of any magnitude is normalized to 1:

$$\int_{-\infty}^{\infty} d(\Delta x_c)\, \phi(x_c - \Delta x_c | \Delta x_c, \Delta t) = 1. \qquad (S2)$$

We expand $P_b(x_c - \Delta x_c, t)$ and $\phi(x_c - \Delta x_c | \Delta x_c, \Delta t)$ in Taylor series about x_c, and truncate the series to first order. We get,

$$P_b(x_c, t + \Delta t) = k_{on}(n_c - n_b)\delta(x_c)\Delta t - k_{off}^{*} P_b(x_c, t)\Delta t + P_b(x_c, t) - \frac{\partial}{\partial x_c}(P_b \overline{\Delta x}_c), \qquad (S3)$$

where the mean clutch extension during a time Δt is

$$\overline{\Delta x}_c(\Delta t) = \int_{-\infty}^{\infty} d(\Delta x_c)\, \Delta x_c \phi(x_c | \Delta x_c, \Delta t) = v_e \Delta t, \qquad (S4)$$

The clutch deformation rate v_e is equal to the difference between the actin retrograde flow velocity and the substrate deformation rate. Rearranging terms in Eq. (S3) and taking the limit $\Delta t \to 0$ allows us to obtain the conservation equation for the probability density

$$\frac{\partial P_b}{\partial t} = k_{on}(n_c - n_b)\delta(x_c) - k_{off}\, e^{\kappa_c x_c / F_b} P_b(x_c, t) - v_e \frac{\partial P_b}{\partial x_c}. \qquad (S5)$$

We have defined $P_b(x_c, t)$ on an infinite domain of clutch extensions to guarantee numerical stability. A negative clutch extension means that the substrate binding domain of the clutch falls behind of its actin binding domain, a phenomenon that we rarely expect to occur in physiological conditions. An equivalent governing equation has been obtained in previous studies (13,14) by using standard mean-field approximations, where they explore steady-state solutions of single protrusions on noncompliant substrates.

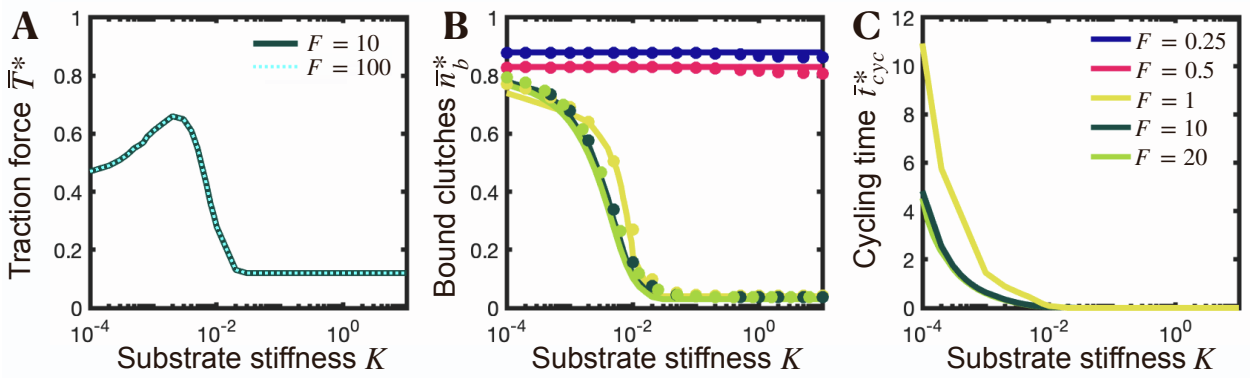

FIGURE S1. Traction force production of individual cellular protrusions exhibit three different regimes: a motor-dominated regime, an intermediate regime, and a clutch-dominated regime. Force transmission is sensitive to substrate compliance — (A) Dimensionless time-averaged traction force, (B) fraction of bound clutches $\bar{n}_b^* = \bar{n}_b/n_c$, and (C) cycling time $\bar{t}_{cyc}^* = \bar{t}_{cyc}k_{off}$ as a function of the dimensionless substrate stiffness K for various values of the myosin activity parameter F. Solid lines are the numerical solution of the mean-field model equations (3) and (4), and circular solid symbols are the mean statistics obtained from the numerical solution of the stochastic model. There is a very good agreement between our mean-field model solution and stochastic model solution. Parameter values: $\tau = 10,\ \omega = 2000$.

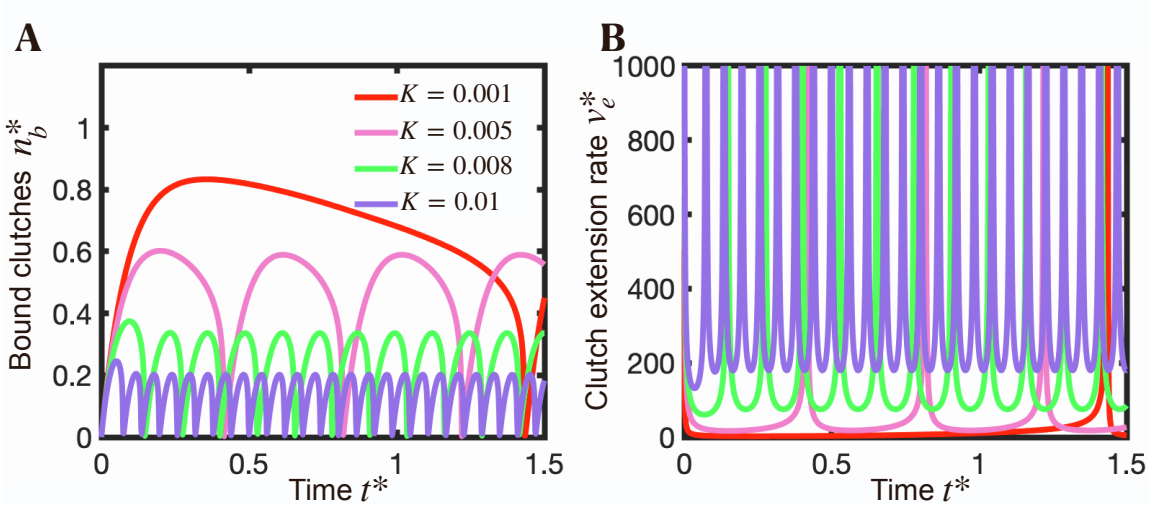

FIGURE S2. Protrusions in the motor-clutch balanced regime display load-and-fail dynamics. Time-evolution of fraction of bound clutches (A) and clutch extension rate (B) obtained by our mean-field model for 4 different substrate stiffnesses. Parameter values: $F = 1,\ \tau = 10,\ \omega = 2000$.

Derivation of the optimum substrate stiffness for maximum traction force

When clutch bonds in the protrusion break before stall conditions are reached, i.e. $t_s^{max} > t_{rupt}$, the protrusion undergoes periods of clutch loading and unloading (load-and-fail behavior). If the substrate is too rigid, the characteristic time for clutches to bind t_{bind} is much larger than the characteristic time for clutches to rupture due to load t_{rupt} ($t_{bind} \gg t_{rupt}$), and clutch bonds break before they have enough time to form large stable adhesions. An early clutch failure cascade thus results in traction forces that are far below their optimum values. If the substrate is too soft, $t_{bind} \ll t_{rupt}$, most of the available clutches mechanically link the actin cytoskeleton with the substrate long before the clutch bonds break by force. Yielding substrates undergo high strain rates that decrease clutch deformation rates, and the protrusion spends most of the clutch loading cycle in a state of low traction force production and high retrograde flow, leading to force transmission far below its optimum value. Therefore, there must exist an intermediate substrate stiffness that maximizes mean traction force production (15,16). An expression for the optimum substrate stiffness was previously derived in (16), where the probability density function of bound clutch forces was assumed to obey a gamma distribution. However, the final expression for the optimum stiffness was only valid for protrusions with balanced number of motors and clutches and was left as a function of an unknown parameter ε, the fraction of the theoretical maximum load that a protrusion can generate. In this work, we relax the adjustable parameter assumption made in (16) and derive a more general expression for the optimum substrate stiffness that is applicable to all motor-clutch ratio regimes. We proceed to estimate the clutch binding time t_{bind} and clutch rupture time t_{rupt} to obtain an analytical expression for the optimum substrate stiffness that

maximizes traction forces. We carry out the mathematical derivation in dimensional form so as not to lose physical intuition throughout the process. We take the zeroth moment of Eq. (1) to obtain the approximated time evolution of the number of bound clutches before clutch bonds break due to load

$$\frac{dn_b}{dt} \approx k_{on} n_c - (k_{on} + k_{off})\, n_b, \qquad t < t_{rupt} \tag{S6}$$

The number of bound clutches thus scales as $n_b \sim (k_{on}/k_{on} + k_{off}) n_c$. The clutch binding time — that is, the characteristic time at which the number of clutches that link the actin cytoskeleton to the extracellular medium reaches equilibrium, scales as $t_{bind} \sim 1/k_{on} + k_{off}$. We define the clutch rupture time t_{rupt} as the ratio between the characteristic clutch rupture length $\ell_{rupt} = F_b/\kappa_c$ and the characteristic clutch extension rate v_{e_c}: $t_{rupt} = \ell_{rupt}/v_{e_c}$. We now proceed to estimate v_{e_c}. Before clutches dissociate due to force, the first-order moment and the clutch extension rate approximately satisfy the following relations

$$\frac{d\ell_b}{dt} \approx v_e n_b - k_{off} \ell_b, \qquad t < t_{rupt}, \tag{S7}$$

$$(\kappa_s + n_b \kappa_c) v_e \approx v_u \kappa_s - \left(\frac{v_u \kappa_s}{n_m F_m} - k_{off}\right) \kappa_c \ell_b, \qquad t < t_{rupt} \tag{S8}$$

where we have used Eq. (2). We take the derivative of Eq. (S8) with respect to time, use Eqs. (S6) and (S8), and rearrange terms to get the following ordinary differential equation for the clutch elongation rate, valid for $t < t_{rupt}$,

$$\frac{dv_e}{dt} + \frac{n_b \kappa_c}{(\kappa_s + n_b \kappa_c)} \left[k_{on} \left(\frac{n_c - n_b}{n_b} \right) + \frac{v_u \kappa_s}{n_m F_m} + k_{off} \left(\frac{\kappa_s}{n_b \kappa_c} - 1 \right) \right] v_e \approx \frac{n_b \kappa_c \kappa_s k_{off} v_u}{(\kappa_s + n_b \kappa_c)^2} \left(1 - \frac{\kappa_s}{n_b \kappa_c} \right). \tag{S9}$$

After a small transient from the onset of loading and for not very rigid substrates, it is expected that enough clutches are mechanically linking substrate and actin filaments so that the substrate rigidity is much smaller than the ensemble clutch stiffness ($\kappa_s \ll n_b \kappa_c$). Under this assumption, Eq. (23) simplifies as

$$\frac{dv_e}{dt} + \left[k_{on}\left(\frac{n_c - n_b}{n_b}\right) + \frac{v_u \kappa_s}{n_m F_m} - k_{off}\right] v_e \approx \frac{\kappa_s k_{off} v_u}{n_b \kappa_c}, \quad t < t_{rupt} \tag{S10}$$

We address the motor-dominated regime and the intermediate regime separately.

Motor-dominated regime

Motor-dominated protrusions operate at optimum conditions when most of the elastic energy in the clutches-substrate axis is taken up at the beginning of the cell cycle by the substrate. Mathematically, this can be expressed as $\kappa_s \gg \kappa_c$. Under these conditions, the substrate deforms at a rate approximately equal to the retrograde flow, the unloaded myosin velocity: $dx_s/dt \sim v_u$ (see Eq. (S17)). The instantaneous traction forces produced at time t therefore scale as $T \sim v_u \kappa_s t$. This implies that first-bound clutch extension evolves as $x_c \sim (v_u \kappa_s/\kappa_c)t$ (see Eq. (S82)), and reaches an extension value equal to its characteristic rupture length $\ell_{rupt} = F_b/\kappa_c$ at a time $t_{rupt}^{single} \sim F_b/v_u \kappa_s$. Notice that the clutch rupture time is independent of clutch stiffness since both rupture length and clutch elongation rate scale inversely to clutch stiffness. The effective clutch binding rate is initially $t_{bind}^{single} \sim 1/n_c k_{on}$. We can determine an upper bound limit of the optimum substrate stiffness that maximizes traction forces κ_s^{opt} by realizing that the necessary condition for the protrusion to operate at its optimum is that clutch binding rates are faster than clutch rupture rates: $t_{rupt}^{single} > t_{bind}^{single}$. Thus, $\kappa_s^{opt} < n_c F_b k_{on}/v_u$. We now proceed to estimate κ_s^{opt}. A careful scaling analysis of Eq. (S10) suggests that in the limit of high motor activity, the clutch extension rate scales as $v_{e_c} \sim \kappa_s v_u (k_{on} + k_{off})/n_c \kappa_c k_{on}$ where we have used Eq. (S6). An increase in the number of available clutches n_c, the clutch stiffness constant κ_c, or the ratio k_{on}/k_{off} reinforces clutches augmenting the clutch resistance against myosin pulling forces, resulting in lower clutch deformation rates. Also, an increase in the load-free velocity of myosin motors results in stronger actin retrograde flows, giving rise to higher clutch extension rates. Because softer substrates undergo higher deformations than more rigid substrates, lower clutch

extension rates are expected for more compliant substrates, as predicted by scaling analysis and in agreement with previous studies (15,17). Our scaling for v_{e_c} implies that the clutch rupture time t_{rupt} scales as $t_{rupt} \sim k_{on} n_c F_b / \kappa_s v_u (k_{on} + k_{off})$. We apply the optimal condition $t_{bind} \sim t_{rupt}$ to determine the substrate stiffness that maximizes traction forces in a motor-dominated protrusion

$$\kappa_{s,m}^{opt} = C_2 \frac{n_c F_b k_{on}}{v_u}, \qquad (S11)$$

Our scaling analysis allows us to obtain the optimum substrate stiffness up to an unknown constant C_2. The upper limit calculated earlier for $\kappa_{s,m}^{opt}$ indicates that $C_2 < 1$. We estimate the constant C_2 by fitting Eq. (S11) to our numerical results. We get $C_2 = 0.4$, consistent with our upper limit calculation. We find very good agreement between our theoretical prediction (Eq. (S11)), the numerical solution of the mean-field model and the solution of the dimensionless version of the stochastic motor-clutch model (17), as shown in Fig. S3, right. According to Eq. (S11), the optimum substrate stiffness is proportional to the characteristic maximum clutch elastic force $n_c F_b$ and inversely proportional to the distance that unloaded actin filaments translocate within the characteristic clutch binding time v_u / k_{on}. Our theoretical solution also suggests that in the high-motor regime, the optimum substrate stiffness is myosin-insensitive and independent of clutch stiffness κ_c.

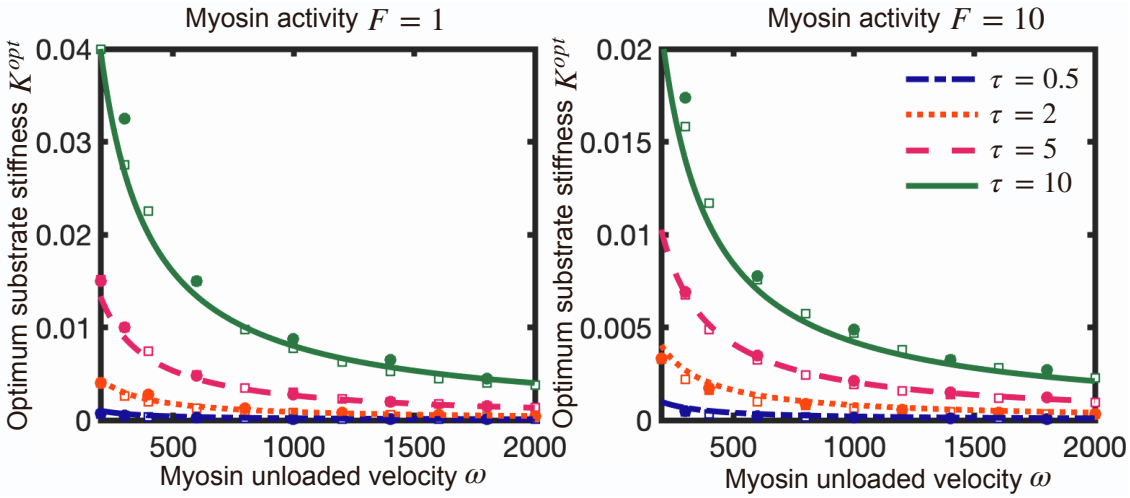

FIGURE S3. Dimensionless optimum substrate stiffness $K^{opt} = \kappa_s^{opt}/n_c\kappa_c$ as a function of the dimensionless myosin load-free velocity ω, for two different values of the myosin activity parameter F. Solid lines correspond to our derived analytical solution (Eq. 6), open symbols correspond to the numerical solution of the mean-field model (Eqs. (3) and (4)), and closed symbols correspond to the numerical solution of the stochastic model.

Motor-clutch balanced regime

In this section, we aim to obtain an expression for the optimum substrate stiffness that maximizes traction forces for protrusions that lie in the intermediate balanced regime. As clutches get stronger either by an increase in the clutch elastic force capacity $n_c F_b$ or an increase in the ratio k_{on}/k_{off}, and/or myosin motors get weaker by a reduction in the total myosin stall force $n_m F_m$, time-averaged actin retrograde flows get weaker, and the characteristic clutch rupture time t_{rupt} increases. This rise in clutch rupture time can be compensated by an increase in substrate stiffness, so that optimum conditions for maximum traction force $t_{bind} \sim t_{rupt}$ are met. Therefore, we expect that as clutches become dominant over motors, the optimum substrate stiffness for traction force will shift towards higher stiffnesses, as previously reported (15,18). We indeed observe this in Fig. 4 as well as in Eq. (6). We go ahead and estimate t_{rupt} from Eq. (S10). Before clutches rupture under load, the clutch strain rate scales as $v_e \sim \kappa_s k_{off} v_u / \left[k_{on}(n_c - n_b)\kappa_c + \frac{n_b \kappa_c v_u \kappa_s}{n_m F_m}\right]$. The characteristic clutch rupture time $t_{rupt} = F_b/\kappa_c v_{e_c}$ scales as $t_{rupt} \sim \frac{k_{on}}{k_{on}+k_{off}} n_c F_b \frac{1}{\kappa_s v_u}\left(1 + C_3 \frac{\kappa_s v_u}{k_{off} n_m F_m}\right)$, where C_3 is an unknown parameter. Notice that our scaling analysis does not allow us to determine this unknown parameter analytically. We apply the condition $t_{bind} \sim t_{rupt}$ to determine the substrate stiffness that maximizes traction forces in a motor-clutch balanced protrusion:

$$\kappa_{s,i}^{opt} = C_2 \frac{n_c F_b k_{on}}{v_u} \frac{1}{1 - C_3 \frac{k_{on}}{k_{off}} \frac{n_c F_b}{n_m F_m}}, \quad (S12)$$

which corresponds with Eq. (6) in the main text. The value of C_3 is obtained by fitting Eq. (S12) with our numerical results. We get $C_3 = 0.05$. Figures 1F and S3 show that our theoretical expression is in very good agreement with our numerical results for all the motor-clutch dimensionless parameters. The optimum substrate stiffness in a protrusion that belongs to the intermediate regime, $\kappa_{s,i}^{opt}$, is myosin sensitive and independent of the effective clutch stiffness κ_c. The optimum substrate stiffness in the motor-dominated regime $\kappa_{s,m}^{opt}$ (Eq. (S11)) is recovered in Eq. (S12) by taking the limit $C_3 k_{on} n_c F_b / k_{off} n_m F_m \to 0$. The optimum stiffness for maximum traction force has been previously estimated and left as a function of an unknown parameter ε, the fraction of the theoretical maximum load that a protrusion can generate (16). This unknown parameter depends on some of the motor-clutch parameters. Equating Eq. (30) in reference (16) with Eq. (S12) in the current study, we find $\varepsilon = e^{-\ln n_c/(F - C_3 \tau)}$. In this derivation, we have assumed that clutch dissociation rates increase exponentially by force according to Bell's law. Protrusions with clutches that have a different lifetime-extension dependence will, in principle, operate at optimum substrate stiffnesses that depend on clutch stiffness.

Critical motor activity parameter that sets the boundary between protrusions in the stalled regime and balanced regime on soft substrates

The boundary between the clutch-dominated stalled regime and the balanced regime is set by the condition $t_s^{max} \sim t_{rupt}$ — that is, the time required to reach stall conditions matches the time needed for clutch bonds to break due to force. The time-evolution of the substrate deformation rate obeys the following ordinary differential equation:

$$\frac{dx_s}{dt} = \frac{\kappa_c}{\kappa_s + n_b \kappa_c} \left[v_u n_b \left(1 - \frac{\kappa_c \ell_b}{n_m F_m} \right) - k_{off} \int_{-\infty}^{\infty} x_c e^{\kappa_c |x_c| / F_b} P_b dx_c \right]. \quad (S13)$$

To estimate the time required for the substrate to reach its maximum deformation t_s^{max}, we approximate the time-evolution equation of the substrate deformation rate for times shorter than the clutch rupture time

$$\frac{dx_s}{dt} \approx \frac{n_b \kappa_c}{\kappa_s + n_b \kappa_c} v_u \left[1 - \left(1 + \frac{n_m F_m k_{off}}{n_b \kappa_c v_u}\right) \frac{x_s}{x_s^{max}}\right] \quad t < t_{rupt} \tag{S14}$$

where the maximum substrate deformation is $x_s^{max} = n_m F_m / \kappa_s$. After a small transient from the onset of loading, we expect that in the clutch dominated regime $n_b \kappa_c v_u \gg n_m F_m k_{off}$. Under this assumption, Eq. (S14) reduces to

$$\frac{dx_s}{dt} \approx \frac{n_b \kappa_c}{\kappa_s + n_b \kappa_c} v_u \left(1 - \frac{x_s}{x_s^{max}}\right), \quad t < t_{rupt} \tag{S15}$$

which suggests that the time to reach maximum substrate deformations t_s^{max} scales as

$$t_s^{max} \sim \frac{\kappa_s + n_b \kappa_c}{n_b \kappa_c} \frac{n_m F_m}{\kappa_s v_u}. \tag{S16}$$

We expect that, after a small transient from the onset of loading, the clutch ensemble stiffness is much more rigid than the substrate stiffness, i.e. $n_b \kappa_c \gg \kappa_s$. We expect this condition to be satisfied if the substrate is soft enough, and sufficient number of clutches are bound. Under this assumption, Eqs. (S15) and (S16) simplify to

$$\frac{dx_s}{dt} \approx v_u \left(1 - \frac{x_s}{x_s^{max}}\right), \quad t < t_{rupt} \tag{S17}$$

$$t_s^{max} \sim \frac{n_m F_m}{\kappa_s v_u}. \tag{S18}$$

We can think of clutches and substrate as two mechanically connected entities, with clutch ensemble stiffness and substrate stiffness $n_b \kappa_c$ and κ_s, respectively. At the time when $n_b \kappa_c \gg \kappa_s$, substrate deformation is much greater than the deformation that any individual clutch undergoes. Consequently, substrates deform at a rate equal to the F-actin retrograde velocity v_{act}, as indicated by Eq. (S17). As long as the system is far away from stall conditions, i.e. $x_s \ll x_s^{max}$, the substrate strain rate is approximately equal to the myosin load-free velocity. The timescale to

reach maximum substrate deformations then scales as $t_s^{max} \sim x_s^{max}/v_u$. The transition between the clutch-dominated regime and the intermediate regime will occur when $t_s^{max} \sim t_{rupt}$ — that is,

$$\frac{n_m F_m}{n_c F_b} \sim \frac{k_{on}}{k_{on} + k_{off}}, \tag{S19}$$

where we have assumed that $n_b \kappa_c \gg \kappa_s$ after a short period of time after the beginning of loading. Therefore, the protrusion will be in the clutch-dominated regime when

$$F < F_{c-i}^{crit} = C_1 \frac{k_{on}}{k_{on} + k_{off}}, \tag{S20}$$

where C_1 is a constant that we estimate by fitting Eq. (S20) with our numerical results. We find $C_1 = 0.4$. The protrusion belongs to the clutch-dominated regime and produces the maximum possible traction force when the ratio between the total myosin stall force $n_m F_m$ and the equilibrium clutch elastic force $n_c F_b k_{on}/(k_{on} + k_{off})$ is lower than a constant of order 1.

Derivation of the mean traction force, number of bound clutches and clutch elongation rates of protrusions on rigid substrates

In our work, we have used two approaches to study the dynamics of cell protrusions: a stochastic Langevin-type approach (17) and a mean-field approach. Whereas the stochastic approach is suitable to a very small timescale, on which stochastic fluctuations in traction forces are observed, the mean-field model addresses a much coarser timescale. On rigid substrates, cycles of loading/unloading occur at a very high frequency. Because the frequency of load-and-fail dynamics is so high, the load-and-fail cycling time is smaller than the minimum timescale addressed by the mean-field model. As a result, the mean-field framework is not able to capture these periodic events on rigid substrates, and its temporal solution reaches steady-state after the first loading event. This allows us to determine the time-averaged traction force $\overline{T}$, mean number of bound clutches $\bar{n}_b$ and mean clutch strain rate $\bar{v}_e$ in a more theoretical way by seeking the steady-state solution of the density conservation equation:

$$\frac{d\overline{P}_b}{dx_c} = \frac{k_{on}(n_c - \bar{n}_b)}{\bar{v}_e}\delta(x_c) - \frac{k_{off}}{\bar{v}_e}\, e^{\frac{\kappa_c|x_c|}{F_b}}\overline{P}_b \tag{S21}$$

where the mean clutch strain rate $\bar{v}_e$ reads

$$\bar{v}_e = v_u\left(1 - \frac{\kappa_c}{n_m F_m}\int_{-\infty}^{\infty} x_c P_b(x_c, t)dx_c\right) \tag{S22}$$

Integration of Eq. (S21) over a small region $x_c \epsilon[-\varepsilon, \varepsilon]$ and taking the limit $\varepsilon \to 0$ yields

$$\overline{P}_b(0^+) = \frac{k_{on}(n_c - \bar{n}_b)}{\bar{v}_e} \tag{S23}$$

where we have assumed that $\overline{P}_b(0^-) \to 0$. We can easily seek a solution for the mean probability density for $x_c > 0$ by applying separation of variables to Eq. (S21) and making use of Eq. (S23) to solve for the integration constant. We find that $\overline{P}_b$ has a double exponential functional form with a very fast decay at a clutch length equal to the clutch rupture length $\ell_{rupt} = F_b/\kappa_c$:

$$\overline{P}_b(x_c) = \frac{k_{on}(n_c - \bar{n}_b)}{\bar{v}_e} e^{\frac{F_b k_{off}}{\kappa_c \bar{v}_e}\left(1 - e^{\frac{\kappa_c}{F_b}x_c}\right)} \tag{S24}$$

Here, $\bar{v}_e$ is still unknown. Taking the zeroth-order moment of Eq. (S24) and rearranging terms, we find

$$\bar{n}_b = \frac{k_{on}\beta}{k_{on}\beta + \bar{v}_e} n_c \tag{S25}$$

where

$$\beta = \frac{F_b}{\kappa_c} e^{\frac{F_b k_{off}}{\kappa_c \bar{v}_e}} \Gamma\left(0, \frac{F_b k_{off}}{\kappa_c \bar{v}_e}\right) \tag{S26}$$

Here, Γ is the incomplete gamma function. Inserting Eq. (S25) into Eq. (S24) yields

$$\overline{P}_b(x_c) = \frac{k_{on}}{k_{on}\beta + \bar{v}_e} n_c e^{\frac{F_b k_{off}}{\kappa_c \bar{v}_e}\left(1 - e^{\frac{\kappa_c}{F_b}x_c}\right)} \tag{S27}$$

We plug Eq. (S27) into Eq. (S21) to obtain a non-linear equation for the mean clutch extension rate

$$\bar{v}_e{}^2 + (k_{on}\beta - v_u)\bar{v}_e + v_u k_{on}\left(\frac{n_c \kappa_c \alpha}{n_m F_m} - \beta\right) = 0 \tag{S28}$$

where

$$\alpha = \left(\frac{F_b}{\kappa_c}\right)^2 e^{\frac{F_b k_{off}}{\kappa_c \bar{v}_e}} G_{2\,3}^{3\,0}\left(\frac{F_b k_{off}}{\kappa_c \bar{v}_e}\middle| \begin{matrix} 1 & 1 \\ 0 & 0 & 0 \end{matrix}\right) \tag{S29}$$

Here, G is the Meijer G-function. We can numerically solve Eq. (S28) to determine $\bar{v}_e$. Once we determine $\bar{v}_e$, we can compute $\bar{n}_b$ and $\bar{P}_b(x_c)$ using Eqs. (S25) and (S27), respectively. The mean traction force can be then obtained as

$$\bar{T} = \frac{G_{2\,3}^{3\,0}\left(\frac{F_b k_{off}}{\kappa_c \bar{v}_e}\middle| \begin{matrix} 1 & 1 \\ 0 & 0 & 0 \end{matrix}\right)}{\Gamma\left(0, \frac{F_b k_{off}}{\kappa_c \bar{v}_e}\right)} \bar{n}_b F_b, \tag{S30}$$

Equation (S30) shows that the mean traction force produced by an individual protrusion on a rigid substrate is proportional to the mean clutch elastic force $\bar{n}_b F_b$ multiplied by a pre-factor that depends on $F_b k_{off}/\kappa_c \bar{v}_e$. We rewrite Eqs. (S24−S30) in dimensionless form:

$$\bar{n}_b^* = \frac{\tau\beta^*}{\tau\beta^* + \bar{v}_e^*}, \qquad \beta^* = \frac{1}{F}\int_0^\infty e^{\frac{1}{F\bar{v}_e^*}(1-e^t)} dt, \qquad \bar{P}_b^*(x_c^*) = \frac{\bar{n}_b^*}{\beta^*} e^{\frac{1}{F\bar{v}_e^*}\left(1-e^{Fx_c^*}\right)} \tag{S31 - S33}$$

$$\bar{v}_e^{*2} + \left(\tau\beta^* - \frac{\omega}{F}\right)\bar{v}_e^* + \frac{\tau\omega}{F}(\alpha^* - \beta^*) = 0, \qquad \alpha^* = \frac{1}{F^2}\int_0^\infty t e^{\frac{1}{F\bar{v}_e^*}(1-e^t)} dt, \qquad \bar{T}^* = F\,\bar{n}_b^* \frac{\alpha^*}{\beta^*} \tag{S34 - S36}$$

We solve for $\bar{v}_e^*$ by numerically solving the nonlinear equation (S34). Once we solve for the mean clutch extension rate, we can compute $\bar{n}_b^*$ and $\bar{T}^*$ using Eqs. (S31) and (S36), respectively. We now proceed to determine analytical expressions for two asymptotic cases: low-motor activity ($F \to 0$) and high-motor activity ($F \to \infty$).

Low-motor activity ($F \to 0$)

We first derive an analytical expression for the dimensionless clutch strain rate $\bar{v}_e^*$. We use regular perturbation theory and expand $\bar{v}_e^*$ in powers of F:

$$\bar{v}_e^* = v_0 + Fv_1 + F^2 v_2 + \mathcal{O}(F^3) \tag{S37}$$

We substitute the assumed perturbation series into Eqs. (S32) and (S33), and after some mathematical manipulation we get:

$$\beta^* = v_0 + F(v_1 - v_0^2) + F^2(2v_0^3 - 2v_0v_1 + v_2) + \mathcal{O}(F^3) \quad (S38)$$

$$\alpha^* = v_0^2 + F(2v_0v_1 - 3v_0^3) + F^2(v_1^2 + 2v_0v_2 - 9v_0^2v_1 + 11v_0^4) + \mathcal{O}(F^3) \quad (S39)$$

We insert Eqs. (S37-S39) into Eq. (S34), and find that the first three leading order terms in the expansion satisfy the following equations:

$$F_0: \quad \tau(v_0 - 1) - 1 = 0, \quad (S40)$$

$$F_1: \quad (\tau + 1)v_0^2 - \omega v_1 + \tau\omega(-3v_0^3 + v_0^2 + 2v_0v_1 - v_1) = 0, \quad (S41)$$

$$F_2: \quad (2 + \tau)v_0v_1 + \tau v_0(v_1 - v_0^2) - \omega v_2 + \tau\omega(v_1^2 + 2v_0v_2 - 9v_0^2v_1 + 11v_0^4) +$$

$$-\tau\omega(2v_0^3 - 2v_0v_1 + v_2) = 0. \quad (S42)$$

The leading-order solution can be easily obtained from Eq. (S40):

$$v_0 = \frac{\tau + 1}{\tau} \quad (S43)$$

We recursively solve for higher order terms by solving Eqs. (S41) and (S42), we get:

$$v_1 = \left(\frac{\tau + 1}{\tau}\right)^2 \left(3 - \frac{1}{\omega}\right) - \frac{\tau + 1}{\tau} \quad (S44)$$

$$v_2 = \frac{\tau + 1}{\tau^3\omega^2}[1 - 9\omega + 7\omega^2 + \tau^2(1 - 6\omega + \omega^2) + \tau(2 - 15\omega + 7\omega^2)] \quad (S45)$$

An expression for the dimensionless time-averaged clutch elongation rate can then be obtained by substituting Eqs. (S43-S45) into the perturbation expansion in Eq. (S37):

$$\bar{v}_e^* = \frac{\tau + 1}{\tau} + \left(\frac{\tau + 1}{\tau}\right)^2 \left(\frac{2\tau + 3}{\tau + 1} - \frac{1}{\omega}\right) F +$$

$$+ \frac{\tau + 1}{\tau^3\omega^2}[1 - 9\omega + 7\omega^2 + \tau^2(1 - 6\omega + \omega^2) + \tau(2 - 15\omega + 7\omega^2)]F^2 + \mathcal{O}(F^3) \quad (S46)$$

Eq. (S43) agrees very well with our numerical solutions as shown in the insets in Fig. 3. In dimensional form, the time-averaged clutch elongation rate reads

$$\bar{v}_e \approx \frac{n_m F_m k_{off}}{n_c \kappa_c}\left(1+\frac{k_{off}}{k_{on}}\right)\left[1+\frac{n_m F_m}{n_c F_b}\left(\left(1+\frac{k_{off}}{k_{on}}\right)\left(3-\frac{F_b k_{off}}{v_u \kappa_c}\right)-1\right)\right] \tag{S47}$$

where we have only kept the first two leading order terms, for simplicity. Equation (S47) indicates that an increase in myosin forces strengthens rearward actin flows, in turn enhancing mean clutch elongation rates. It also indicates that an increase in the total number of clutches n_c, the clutch stiffness κ_c, the clutch association constant k_{on}, or the characteristic clutch rupture force F_b decreases averaged clutch elongation rates by strengthening clutches, whereas an increase in the myosin load-free velocity v_u or in the unloaded clutch dissociation constant k_{off} increases clutch extension rates. Because only large values of ω are physiologically relevant, we can simplify Eq. (S47) by taking the limit for large ω. We get,

$$\bar{v}_e^*(\omega \to \infty) = \frac{\tau+1}{\tau}\left[1+\frac{2\tau+3}{\tau}F+\frac{7+7\tau+\tau^2}{\tau^2}F^2\right]+\mathcal{O}(F^3) \tag{S48}$$

Next, we seek a solution for the time-averaged fraction of bound clutches. We substitute the results obtained in Eqs. (S43–S45) into Eqs. (S38) and (S39), and plug the results for β^* and α^* along with Eq. (S46) into Eq. (S31); upon simplification, we get:

$$\bar{n}_b^* = \frac{\tau}{\tau+1}-\frac{1}{\tau+1}F+\frac{1-\omega}{\tau\omega}F^2+\mathcal{O}(F^3) \tag{S49}$$

Very good agreement is found between Eq. (S49) and our numerical results, as shown in Fig. 3, middle. In dimensional form, the time-averaged number of bound clutches reads

$$\bar{n}_b \approx \frac{k_{on}}{k_{on}+k_{off}}\left(n_c-\frac{n_m F_m}{F_b}\frac{k_{off}}{k_{on}}+\frac{(n_m F_m)^2}{n_c F_b^2}\right) \tag{S50}$$

where we have only kept the first two leading order terms, for simplicity. The leading order term in Eq. (S50) corresponds to the equilibrium number of bound clutches in an unloaded state, set by just a balance of binding/unbinding kinetics. As expected, an increase in myosin forces reduces the time-averaged number of bound clutches, as indicated by the negative sign in front of the second term in Eq. (S50). The first two leading order terms do not depend on the parameter ω.

Therefore, we must look at the F^2 term in Eq. (S49) to study the dependence of number of bound clutches on clutch stiffness κ_c and myosin-load free velocity v_u. We find that larger values of κ_c or v_u (larger ω) leads to a reduction in the average number of bound clutches, consistent with our discussion of Fig. 2 in the main text and with Fig. S4, right. Finally, we seek a formula for the time-averaged traction force. We substitute Eqs. (S38), (S39) and (S49) into Eq. (S36) and simplify, to get

$$\bar{\mathrm{T}}^* = \mathrm{F} - \frac{\tau+1}{\tau\omega}\mathrm{F}^2 + \frac{1+2\tau+\tau^2-\omega(3+5\tau+2\tau^2)}{\omega^2\tau^2}\mathrm{F}^3 + \mathcal{O}(\mathrm{F}^4) \qquad \text{(S51)}$$

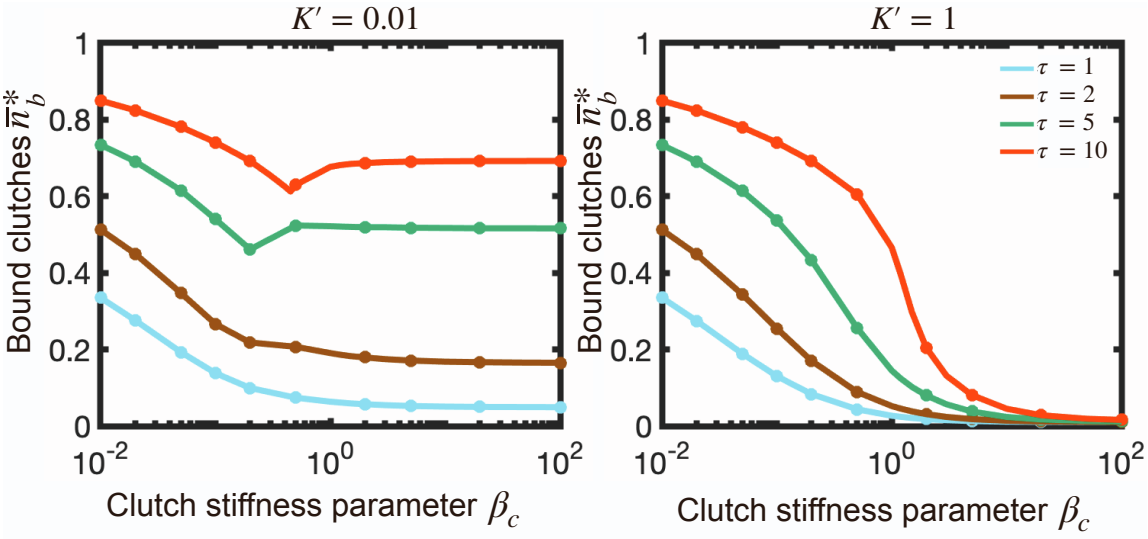

FIGURE S4. Time-averaged fraction of bound clutches as a function of the clutch stiffness parameter β_c for different values of the clutch kinetic parameter τ and for two values of the substrate stiffness parameter K' ($\mathrm{K} = \mathrm{K}'/\beta_c$): (left) $\mathrm{K}' = 0.01$ and (right) $\mathrm{K}' = 1$. Parameter values: $\mathrm{F} = 1$, $\omega' = 200$ ($\omega = \omega'\beta_c$). Notice that $\kappa_c \propto \beta_c$.

The leading order traction force term in Eq. (S51) corresponds to the total myosin stall force, the maximum available force. The second leading order term in Eq. (S51) indicates that as the number of motors increase, the traction force negatively deviates from the total myosin stall force. An increase in the number of clutches n_c, the clutch stiffness κ_c, the clutch association rate

constant, k_{on}, and the myosin load-free velocity, v_u, increases the production of traction forces, whereas an increase in the unloaded clutch dissociation rate constant, k_{off}, negatively contributes to traction force production. Among all the parameters, the least obvious dependence is that of traction force on myosin load-free velocity. On rigid substrates, actomyosin pulling forces mainly deform molecular clutches, as rigid substrates barely undergo any deformation. In low-motor protrusions, adhesions build strong clusters that inhibit retrograde flows that result in lower clutch loading rates. Consequently, clutches dissociate stochastically before reaching their rupture length giving rise to poor force transmission. A higher value of v_u allows clutches to work at their fullest capacity, resulting in stronger retrograde flows, thus higher time-averaged traction forces. In dimensional form, the time-averaged traction force reads

$$\overline{T} \approx n_m F_m \left[1 - \frac{n_m F_m k_{off}^2}{n_c \kappa_c v_u k_{on}} \left(1 + \frac{k_{on}}{k_{off}} + \frac{\kappa_c v_u}{k_{on} F_b} \left(1 + 2\frac{k_{on}}{k_{off}}\right)\right)\right] \tag{S52}$$

where we have only kept the first two leading order terms, for simplicity.

High-motor activity ($F \to \infty$)

We proceed now to obtain analytical expressions for $\overline{T}$, $\bar{n}_b$ and $\bar{v}_e$ for motor-dominated protrusions. At high motor activity, time-averaged traction force and number of bound clutches are independent of motor activity, as demonstrated by the plateau in Figs. 3A and 3B for large F. We take the limit $F \to \infty$ in Eq. (S34) and look for the leading-order term, we get

$$(\bar{v}_e^* + \tau\beta^*)\left(\bar{v}_e^* - \frac{\omega}{F}\right) \to 0. \tag{S53}$$

Only positive values of $\bar{v}_e^*$ are physically possible, thus solution of Eq. (S53) reads

$$\bar{v}_e^* \to \frac{\omega}{F} \tag{S54}$$

Therefore, clutches of motor-dominated protrusions elongate on rigid substrates at an average rate that approaches the myosin load-free velocity $\bar{v}_e = v_u$. The mean number of bound clutches

of a motor-dominated protrusion can then be obtained by plugging Eq. (S32) into Eq. (S31) and making use of Eq. (S54), we get:

$$\bar{n}_b^* \to \frac{\tau e^{\frac{1}{\omega}} \Gamma\left(0, \frac{1}{\omega}\right)}{\tau e^{\frac{1}{\omega}} \Gamma\left(0, \frac{1}{\omega}\right) + \omega} \tag{S55}$$

Equation (S55) is in very good agreement with the stochastic model results, as shown in Fig. 4C. The fraction of bound clutches monotonically increases as the clutch kinetic parameter τ increases and/or the parameter ω decreases. In dimensional form, Eq. (S55) reads

$$\bar{n}_b \to \frac{k_{on} F_b e^{\frac{F_b k_{off}}{\kappa_c v_u}} \Gamma\left(0, \frac{F_b k_{off}}{\kappa_c v_u}\right)}{k_{on} F_b e^{\frac{F_b k_{off}}{\kappa_c v_u}} \Gamma\left(0, \frac{F_b k_{off}}{\kappa_c v_u}\right) + v_u \kappa_c} n_c, \tag{S56}$$

Finally, we can easily obtain the time-averaged force transmitted to the substrate:

$$\bar{T}^* \to \frac{G_{2\,3}^{3\,0}\left(\frac{1}{\omega} \middle| \begin{matrix} 1 & 1 \\ 0 & 0 \end{matrix} \; 0\right)}{\Gamma\left(0, \frac{1}{\omega}\right)} \bar{n}_b^* \tag{S57}$$

This solution has also been derived in prior publications (13,19). It is worth mentioning that this solution is only valid for high motor activity. In dimensional form, Eq. (S57) reads

$$\bar{T} \to \frac{G_{2\,3}^{3\,0}\left(\frac{F_b k_{off}}{\kappa_c v_u} \middle| \begin{matrix} 1 & 1 \\ 0 & 0 \end{matrix} \; 0\right)}{\Gamma\left(0, \frac{F_b k_{off}}{\kappa_c v_u}\right)} \bar{n}_b F_b, \tag{S58}$$

where $\bar{n}_b$ is that in Eq. (S56).

Derivation of the mean traction force produced by cell protrusions with reinforcement on rigid substrates

The frequency of load-and-fail dynamics is so high on rigid substrates that the mean-field framework cannot capture these periodic events and the mean-field temporal solution reaches steady-state after the first loading event. This steady-solution corresponds to the time-averaged

solution of the stochastic motor-clutch model, allowing us to determine the time-averaged traction force $\bar{T}$, mean number of bound clutches $\bar{n}_b$ and mean clutch strain rate $\bar{v}_e$ in a more theoretical way by seeking the steady-state solution of Eq. (7). The time-averaged probability density of clutch extensions for a protrusion with clutch reinforcement has also a double exponential form on clutch extensions:

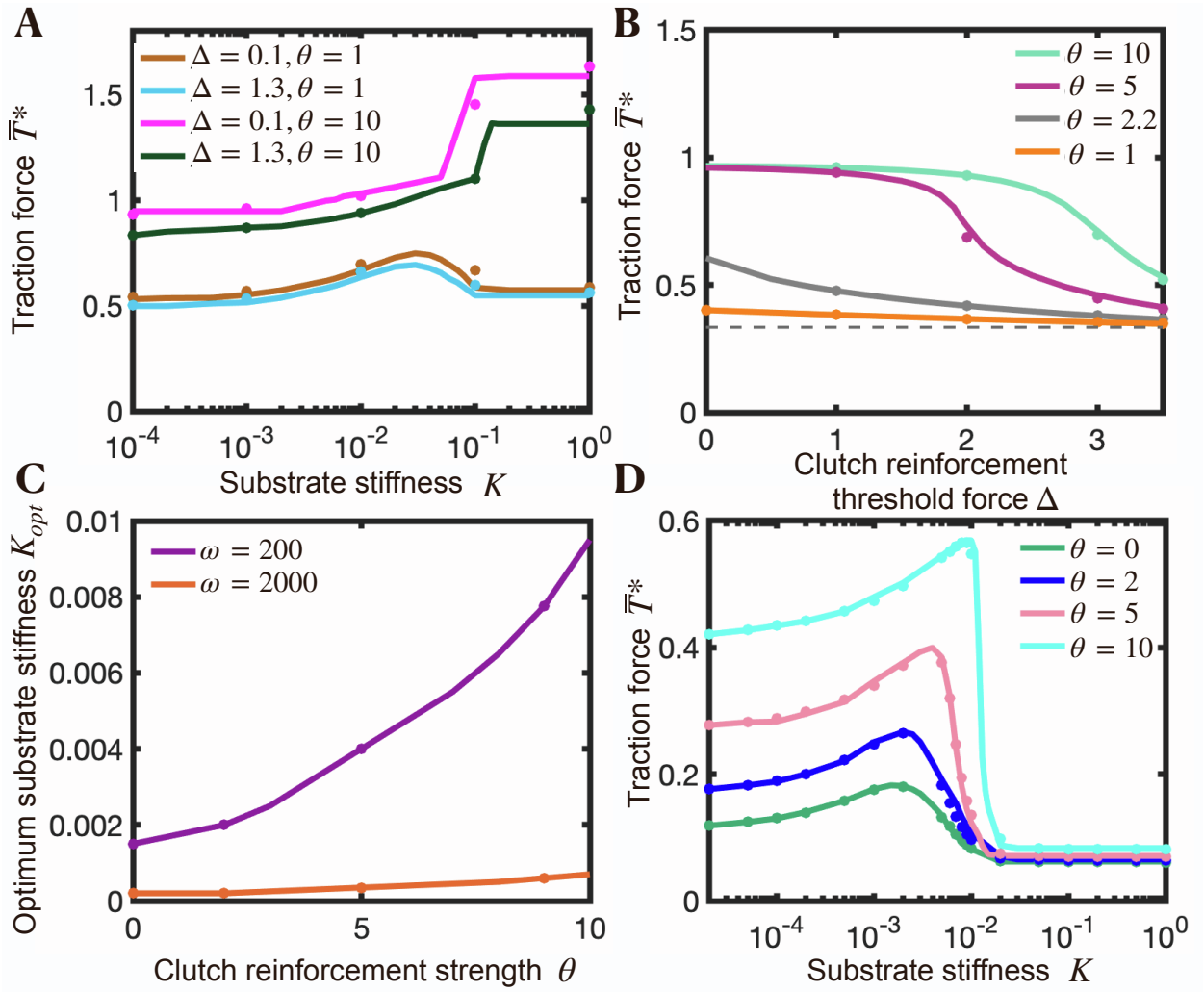

FIGURE S5. Load-dependent clutch reinforcement shifts the optimum substrate stiffness for maximal force transmission to stiffer substrates. (A) Dimensionless time-averaged traction force as a function of substrate stiffness for two values of the clutch reinforcement parameter θ and clutch reinforcement threshold force Δ. Parameter values: $\tau = 1$, $\omega = 2000$, $F = 10$. (B) Dimensionless time-averaged traction force on rigid substrates ($K \to \infty$) as a function of the

dimensionless clutch reinforcement threshold force Δ for four different values of the clutch reinforcement parameter. Dashed gray line corresponds to the force transmission curve in the absence of clutch reinforcement ($\theta = 0$). Parameter values: $\omega = 200, F = 10, \tau = 5$. (C) Optimum substrate stiffness as a function of the clutch reinforcement parameter for two different values of the dimensionless myosin unloaded velocity ω. Solid lines are the numerical solution of the developed mean-field model (Eq. S68) and symbols are the numerical solutions of the stochastic motor-clutch model. Parameter values: $\omega = 200, F = 1, \tau = 1$. (D) Dimensionless time-averaged traction force as a function of the dimensionless substrate stiffness for four different values of the clutch reinforcement parameter θ. Parameter values: $\omega = 200, F = 1, \tau = 1, \Delta = 0$.

$$\bar{P}_b(x_c) = \frac{k_{on}\left(1 + \theta\frac{\bar{n}_b}{n_c}\right)(n_c - \bar{n}_b)}{\bar{v}_e} e^{\frac{F_b k_{off}}{\kappa_c \bar{v}_e}\left(1 - e^{\frac{\kappa_c}{F_b}x_c}\right)}. \tag{S59}$$

where we have assumed in the subsequent derivation that the clutch reinforcement threshold force is $F_{th} = 0$. The mean clutch strain rate and mean number of bound clutches take the form:

$$\bar{v}_e = v_u\left[1 - \frac{\kappa_c k_{on}}{n_m F_m \bar{v}_e}\left(1 + \theta\frac{\bar{n}_b}{n_c}\right)(n_c - \bar{n}_b)\sigma\right] \tag{S60}$$

and

$$\bar{n}_b = \frac{k_{on}(1 + \theta\frac{\bar{n}_b}{n_c})(n_c - \bar{n}_b)}{\bar{v}_e}\rho \tag{S61}$$

where

$$\sigma = \int_0^\infty e^{\frac{F_b k_{off}}{\kappa_c \bar{v}_e}\left(1 - e^{\frac{\kappa_c}{F_b}x_c}\right)} x_c dx_c, \tag{S62}$$

and

$$\rho = \int_0^\infty e^{\frac{F_b k_{off}}{\kappa_c \bar{v}_e}\left(1 - e^{\frac{\kappa_c}{F_b}x_c}\right)} dx_c \tag{S63}$$

We can express $\bar{n}_b$ as function of $\bar{v}_e$ by rearranging terms in Eq. (S61):

$$\bar{n}_b = \frac{n_c}{2\theta}\left[-\left(\frac{\bar{v}_e}{k_{on}\rho} + 1 - \theta\right) + \sqrt{\left(\frac{\bar{v}_e}{k_{on}\rho} + 1 - \theta\right)^2 + 4\theta}\right] \tag{S64}$$

We plug Eq. (S64) into Eq. (S60) and obtain a nonlinear integral equation for the mean clutch extension rate:

$$1 - \frac{\bar{v}_e}{v_u} + \frac{\kappa_c \sigma n_c}{2\theta n_m F_m \rho}\left[\left(\frac{\bar{v}_e}{k_{on}\rho} + 1 - \theta\right) - \sqrt{\left(\frac{\bar{v}_e}{k_{on}\rho} + 1 - \theta\right)^2 + 4\theta}\right] = 0 \tag{S65}$$

The traction force produced by the protrusion can then be expressed as

$$\bar{T} = \frac{\kappa_c \bar{n}_b \sigma}{\rho} \tag{S66}$$

In dimensionless form, Eqs. (S64−S66) read:

$$\bar{n}_b^* = \frac{1}{2\theta}\left[-\left(\frac{\bar{v}_e^*}{\tau\rho^*} + 1 - \theta\right) + \sqrt{\left(\frac{\bar{v}_e^*}{\tau\rho^*} + 1 - \theta\right)^2 + 4\theta}\right] \tag{S67}$$

$$4\theta^2 \rho^{*2}\left(1 - \frac{F}{\omega}\bar{v}_e^*\right)^2 + 4\theta\sigma^*\left[\left(1 - \frac{F}{\omega}\bar{v}_e^*\right)\left(\frac{\bar{v}_e^*}{\tau} + \rho^*(1-\theta)\right) - \sigma^*\right] = 0 \tag{S68}$$

$$\bar{T}^* = \frac{F\bar{n}_b^*\sigma^*}{\rho^*} \tag{S69}$$

where

$$\sigma^* = \frac{n_c^2\kappa_c^2}{n_m^2 F_m^2}\int_0^\infty e^{\frac{F_b k_{off}}{\kappa_c \bar{v}_e}\left(1 - e^{\frac{\kappa_c}{F_b}x_c}\right)} x_c dx_c, \quad \rho^* = \frac{n_c\kappa_c}{n_m F_m}\int_0^\infty e^{\frac{F_b k_{off}}{\kappa_c \bar{v}_e}\left(1 - e^{\frac{\kappa_c}{F_b}x_c}\right)} dx_c$$

Notice that $\rho^* = \rho n_c \kappa_c / n_m F_m$ and $\sigma^* = \sigma n_c^2 \kappa_c^2 / n_m^2 F_m^2$. We solve Eq. (S68) numerically and find that clutch reinforcement significantly enhances traction force generation on rigid substrates for protrusions with fast clutch association kinetics (large τ), as shown in Fig. S6A. As the clutch reinforcement parameter θ increases, the time-averaged traction force produced by the protrusion rises, and it eventually reaches a plateau at large values of θ, where the protrusion nearly reaches stall conditions, as shown in Fig. S6A for $\tau = 3$ and $\tau = 5$. Our mean-field model results with clutch reinforcement show that adhesion reinforcement shifts the optimum unloaded velocity parameter

to larger values (Fig. S6B). We also find that clutch reinforcement on rigid substrates shifts the optimum clutch stiffness to higher stiffnesses, as Fig. S6C shows. Interestingly, the shifts in the optimum unloaded velocity parameter and clutch stiffness are very sensitive to changes in the clutch reinforcement parameter θ for the largest values of the clutch kinetic parameter τ explored, whereas they are nearly independent of θ for the smallest value of τ explored ($\tau = 1$), as Figs. S6B and S6C show, respectively.

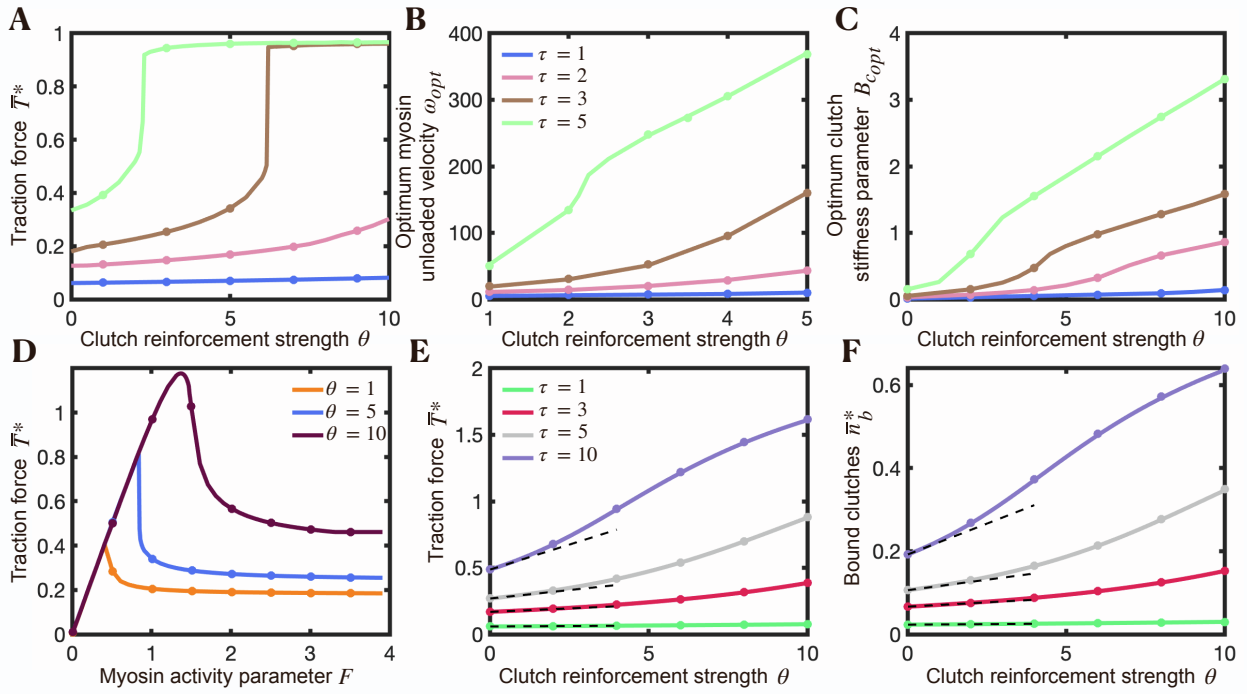

FIGURE S6. Load-dependent clutch reinforcement on rigid substrates shifts the optimum unloaded velocity parameter and optimum clutch stiffness to larger values. (A) Time-averaged traction force (parameter values: $\mathrm{F} = 1, \omega = 200, \mathrm{K} \to \infty$), (B) optimum unloaded velocity parameter (parameter values: $\mathrm{F} = 1, \mathrm{K} \to \infty$), and (C) optimum clutch stiffness parameter (parameter values: $\mathrm{F} = 1, \omega' = 200, \mathrm{K}' = 1$) as a function of the clutch reinforcement parameter θ for four different values of the clutch kinetic parameter τ. Notice that $\mathrm{K} = \mathrm{K}'/\beta_c$ and $\omega = \omega'\beta_c$. Solid lines are the numerical solution of the mean-field model (Eq. S68) and symbols are the numerical solutions of the stochastic motor-clutch model. (D) Time-averaged traction force as a function the myosin activity parameter F for three different values of the clutch reinforcement

parameter. Parameter values: $\tau = 3,\ \omega = 200,\ \mathrm{K} \to \infty$. Solid lines are the numerical solution of the mean-field model (Eq. S68) and symbols are the numerical solutions of the stochastic motor-clutch model. (E) Time-averaged traction force and (F) number of bound clutches as a function of the clutch reinforcement parameter for four different values of the clutch kinetic parameter. Parameter values: $\mathrm{F} \to \infty,\ \mathrm{K} \to \infty, \omega = 200$. Solid lines correspond to our analytical solutions (Eqs. (S70) and (S71)), symbols correspond to the numerical solutions of the stochastic motor-clutch model, and black dashed lines are the asymptotic solutions for small θ obtained in Eqs. (S71) and (S73). Δ=0 in all panels.

The sensitivity of force transmission on the parameter θ for different myosin activity levels is quantified in Fig. S6D. We find that low-motor activity protrusions (small F) produce θ-independent traction forces, since the protrusion is already operating at stall conditions. High-motor activity protrusions (large F) display high-frequency load-and-fail dynamics on rigid substrates, and force transmission and mean number of bound clutches are enhanced as the clutch reinforcement parameter increases, as shown in Figs. S6D, S6E and S6F.

We further proceed to obtain asymptotic expressions for the time-averaged traction force and mean number of bound clutches for motor-dominated protrusions with reinforcement. The leading order term can be obtained by taking the limit $\mathrm{F} \to \infty$ on Eqs. (S59−S69). After some math, we get:

$$\bar{n}_b^* \to \frac{-\left(\frac{\omega}{\tau e^{1/\omega}\Gamma(0,1/\omega)} + 1 - \theta\right) + \sqrt{\left(\frac{\omega}{\tau e^{1/\omega}\Gamma(0,1/\omega)} + 1 - \theta\right)^2 + 4\theta}}{2\theta} \tag{S70}$$

$$\bar{T}^* \to \frac{G_{2\,3}^{3\,0}\left(\frac{1}{\omega}\middle|\begin{matrix}1 & 1\\ 0 & 0 & 0\end{matrix}\right)}{\Gamma\left(0,\frac{1}{\omega}\right)}\bar{n}_b^* \tag{S71}$$

$$\bar{P}_b^*(x_c^*) \to \frac{F\tau}{\omega}\left(1 + \theta\frac{\bar{n}_b^*}{n_c}\right)(1 - \bar{n}_b^*)e^{\frac{1-e^{Fx_c^*}}{\omega}} \tag{S72}$$

Our analytical solutions (Eqs. S70-S72) are in very good agreement with the stochastic motor-clutch model solutions, as shown in Figs. S6E and S6F. We find that high-motor protrusions on rigid substrates can avoid frictional slippage and produce large traction forces provided that the clutch parameters θ and/or τ are sufficiently large and the parameter ω is sufficiently small, as shown in Figs. S6E and (6).

We additionally take the limit of Eq. (S70) when $\theta \to 0$ to explore traction force generation on protrusions with low reinforcement. We get:

$$\bar{n}_b^* \to \frac{1}{1+\frac{\omega}{\tau e^{1/\omega}\Gamma(0,1/\omega)}} + \frac{\frac{\omega}{\tau e^{1/\omega}\Gamma(0,1/\omega)}}{\left(1+\frac{\omega}{\tau e^{1/\omega}\Gamma(0,1/\omega)}\right)^3}\theta \qquad (S73)$$

where we have only kept the first two leading order terms in θ, for simplicity. The positive sign in front of the last term in Eq. (S73) indicates that reinforcement enhances the mean number of bound clutches and, therefore, the mean traction force produced by the protrusion as shown in Figs. S6E and S6F.

Dynamics of strong-motor protrusions are myosin independent

In this section, we demonstrate using a simple approach that clutch dynamics of strong-motor protrusions do not depend on myosin activity. We explore the evolution of an individual protrusion right after the first clutch connects the actin-cytoskeleton with the surrounding substrate. Before any clutch couples the actin network with the substrate, the actin cytoskeleton flows rearwards at the myosin load-free velocity. Once the first clutch binds, force balance reads

$$n_m F_m \left(1-\frac{v_{act}}{v_u}\right) = \kappa_c x_c = \kappa_s x_s. \qquad (S74)$$

The clutch extension rate is equal to the difference between actin retrograde flow velocity and the substrate deformation rate:

$$\frac{dx_c}{dt} = v_{act} - \frac{dx_s}{dt}. \tag{S75}$$

Combination of Eqs. (S74) and (S75) yields an ordinary differential equation for the actin retrograde flow velocity:

$$\frac{n_m F_m}{v_u}\left(\frac{1}{\kappa_c} + \frac{1}{\kappa_s}\right)\frac{dv_{act}}{dt} = -v_{act}. \tag{S76}$$

We easily solve for Eq. (S76) by applying separation of variables:

$$v_{act}(t) = v_u e^{-\frac{v_u}{n_m F_m\left(\frac{1}{\kappa_c}+\frac{1}{\kappa_s}\right)}t} \tag{S77}$$

We substitute Eq. (S77) into Eq. (S74) to obtain:

$$x_c(t) = \frac{\kappa_s}{\kappa_c}x_s(t) = \frac{n_m F_m}{\kappa_c}\left(1 - e^{-\frac{v_u}{n_m F_m\left(\frac{1}{\kappa_c}+\frac{1}{\kappa_s}\right)}t}\right) \tag{S78}$$

If the bound clutch does not dissociate before reaching its characteristic rupture length $x_c^{rupt} = F_b/\kappa_c$ and that no other clutch binds, Eq. (S78) implies that the time required for the clutch to reach its rupture length t_r is:

$$t_r = -\frac{n_m F_m}{v_u}\left(\frac{1}{\kappa_c} + \frac{1}{\kappa_s}\right)\ln\left(1 - \frac{F_b}{n_m F_m}\right). \tag{S79}$$

Notice that the argument of the logarithm in Eq. (S79) is positive provided that the characteristic clutch rupture length x_c^{rupt} is smaller than the clutch elongation at stall conditions $x_c^{stall} = n_m F_m/\kappa_c$. Therefore, Eq. (S79) is valid for $x_c^{rupt} < x_c^{stall}$. We take the high-myosin limit ($n_m F_m \to \infty$) of Eqs. (S78) and (S79) to obtain

$$\lim_{n_m F_m \to \infty} x_c(t) = \frac{v_u t}{1 + \kappa_c/\kappa_s}\left[1 - \frac{v_u t}{2 n_m F_m\left(\frac{1}{\kappa_c} + \frac{1}{\kappa_s}\right)}\right] + \mathcal{O}\left(\frac{t^3}{(n_m F_m)^2}\right), \tag{S80}$$

$$\lim_{n_m F_m \to \infty} t_r = \frac{F_b}{v_u}\left(\frac{1}{\kappa_c} + \frac{1}{\kappa_s}\right) + \mathcal{O}\left(\frac{1}{n_m F_m}\right). \tag{S81}$$

Eq. (S81) suggests that, in the high-myosin limit and for times on the order of the clutch rupture time $t = \mathcal{O}(t_r)$, clutch elongation is asymptotically myosin independent. Hence, the clutch elongation rate is time independent and asymptotically equal to

$$\lim_{n_m F_m \to \infty} \frac{dx_c(t)}{dt} = \frac{v_u}{1 + \kappa_c/\kappa_s}. \tag{S82}$$

We use Eqs. (S74) and (S82) to obtain the asymptotic substrate deformation rate:

$$\lim_{n_m F_m \to \infty} \frac{dx_s(t)}{dt} = \frac{v_u}{1 + \kappa_s/\kappa_c}, \tag{S83}$$

which indicates that the dynamics of motor-dominated protrusions are myosin insensitive, in agreement with our numerical and analytical results. Notice that the average time required for a second clutch to bind is equal to $1/(n_c - 1)k_{on}$. A second clutch will on average bind before the first bound clutch reaches its rupture length when

$$\frac{F_b k_{on}(n_c - 1)}{v_u}\left(\frac{1}{\kappa_c} + \frac{1}{\kappa_s}\right) > 1. \tag{S84}$$

Numerical solution of the mean-field conservation equation

We solve Eqs. (3-4) of the main text numerically for a range of parameter values. Note that the probability density $P_b^*(x_c^*, t^*)$ is defined on an infinite domain on clutch extensions. We use a sufficiently large computational domain so that domain size does not affect the numerical solution. We impose that the probability density vanishes at the two boundaries, i.e. $P_b^*(\pm\infty, t^*) = 0$. We discretize the domain using a uniform grid, approximate integrals using the trapezoidal quadrature method, and approximate the first derivative in Eq. (3) using the first order left-sided finite difference scheme to guarantee numerical stability. We approximate the Dirac delta function with the following function:

$$\delta^*(x_c^*) \approx \frac{1}{\pi}\frac{\varepsilon}{x_c^{*2} + \varepsilon^2}, \tag{S85}$$

where we have used $\varepsilon = 5 \times 10^{-3}$ in all simulations. We have integrated Eq. (3) in time by using the Forward-Backward Euler method, where we have treated the clutch binding term explicitly, and the clutch unbinding and clutch extension terms implicitly.

Clutches with catch bond properties enhance traction forces

In this section, we proceed to explore the effect of catch bond adhesion properties on force transmission. We follow the assumption made in (15) and assume that both catch and slip bond dissociation kinetics depend exponentially on clutch force. Therefore, the conservation equation for the probability density now reads:

$$\frac{\partial P_b}{\partial t} = k_{on}(n_c - n_b)\delta(x_c) - \left(k_{off}\, e^{\frac{\kappa_c|x_c|}{F_b}} + k_{off}^{catch} e^{-\frac{\kappa_c|x_c|}{F_b^{catch}}}\right)P_b - v_e\frac{\partial P_b}{\partial x_c}, \tag{S86}$$

where k_{off} and k_{off}^{catch} are the unloaded clutch slip and catch bond dissociation rates, respectively, and F_b and F_b^{catch} are the characteristic forces of the slip and catch bonds, respectively. In dimensionless form, Eq. (S86) reads

$$\frac{\partial P_b^*}{\partial t^*} = \tau(1 + \theta n_b^*)(1 - n_b^*)\delta^*(x_c^*) - \left(e^{F|x_c^*|} + K_{off}\, e^{-\frac{F|x_c^*|}{\chi_b}}\right)P_b^* - v_e^*\frac{\partial P_b^*}{\partial x_c^*}, \tag{S87}$$

where we have introduced two additional dimensionless numbers:

$$K_{off} = \frac{k_{off}^{catch}}{k_{off}}, \qquad \chi_b = \frac{F_b^{catch}}{F_b} \tag{S88}$$

The dimensionless clutch strain rate v_e^* appearing in Eq. (S87) have been previously introduced in Eq. (S34). The numerical solution of Eq. (S87) is shown in Fig. S7. For low values of the parameter ω, force transmission depends inversely on the parameter χ_b for the whole range of substrate stiffnesses, since the effective clutch dissociation rate at low clutch extensions scales with χ_b due to catch bond behavior. For high values of the parameter ω, force transmission is only sensitive to changes in the parameter χ_b for protrusions on soft enough substrate stiffnesses. On

sufficiently rigid substrates, clutch loading is fast, slip bonds break by force, and the protrusion undergoes frictional slippage. Interestingly, the optimum substrate stiffness for maximal force transmission is not sensitive to the changes in the catch bond force parameter χ_b, as shown in Fig. S7.

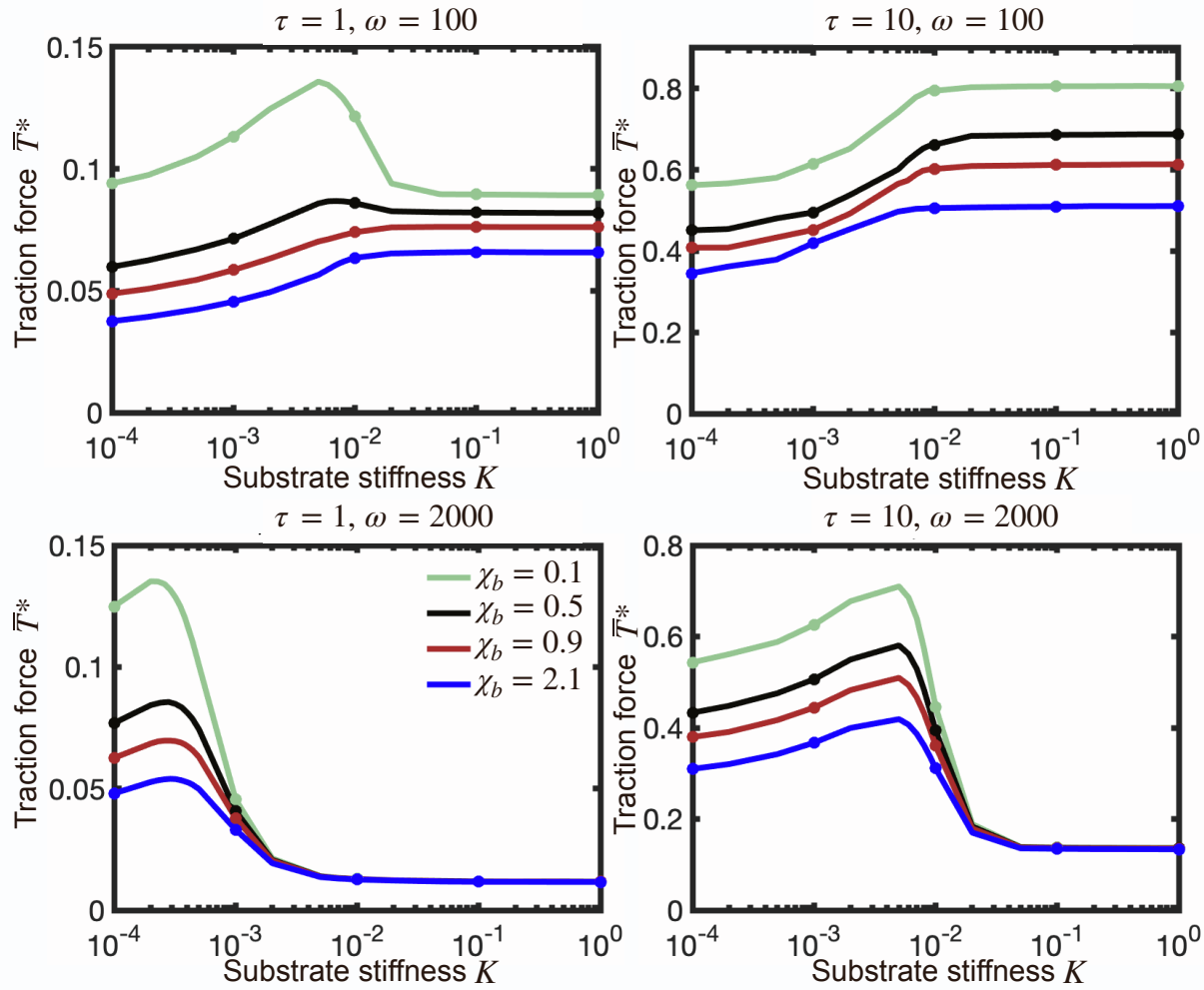

FIGURE S7. Optimum substrate stiffness for maximal for transmission is independent of the catch bond force parameter χ_b. Time-averaged traction force as a function of substrate stiffness for four different values of χ_b. Parameter values: $F = 1, K_{off} = 20$. Solid lines correspond to the mean-field numerical solution (Eq. (S87)) and symbols correspond to the numerical solutions of the stochastic motor-clutch model.

REFERENCES

1. Pollard, T. D., and B. O'Shaughnessy. 2019. Molecular Mechanism of Cytokinesis. *Annu Rev Biochem*. 88:661-689, doi: 10.1146/annurev-biochem-062917-012530, https://www.ncbi.nlm.nih.gov/pubmed/30649923.
2. Litvinov, R. I., A. Mekler, H. Shuman, J. S. Bennett, V. Barsegov, and J. W. Weisel. 2012. Resolving two-dimensional kinetics of the integrin αIIbβ3-fibrinogen interactions using binding-unbinding correlation spectroscopy. *J Biol Chem*. 287(42):35275-35285, doi: 10.1074/jbc.M112.404848, https://www.ncbi.nlm.nih.gov/pubmed/22893701.
3. Elosegui-Artola, A., E. Bazellières, M. D. Allen, I. Andreu, R. Oria, R. Sunyer, J. J. Gomm, J. F. Marshall, J. L. Jones, X. Trepat, and P. Roca-Cusachs. 2014. Rigidity sensing and adaptation through regulation of integrin types. *Nat Mater*. 13(6):631-637, doi: 10.1038/nmat3960, https://www.ncbi.nlm.nih.gov/pubmed/24793358.
4. Jiang, G., G. Giannone, D. R. Critchley, E. Fukumoto, and M. P. Sheetz. 2003. Two-piconewton slip bond between fibronectin and the cytoskeleton depends on talin. *Nature*. 424(6946):334-337, doi: 10.1038/nature01805, https://www.ncbi.nlm.nih.gov/pubmed/12867986.
5. Yao, M., B. T. Goult, B. Klapholz, X. Hu, C. P. Toseland, Y. Guo, P. Cong, M. P. Sheetz, and J. Yan. 2016. The mechanical response of talin. *Nat Commun*. 7:11966, doi: 10.1038/ncomms11966, https://www.ncbi.nlm.nih.gov/pubmed/27384267.
6. Chen, Y., H. Lee, H. Tong, M. Schwartz, and C. Zhu. 2017. Force regulated conformational change of integrin α. *Matrix Biol*. 60-61:70-85, doi: 10.1016/j.matbio.2016.07.002, https://www.ncbi.nlm.nih.gov/pubmed/27423389.
7. del Rio, A., R. Perez-Jimenez, R. Liu, P. Roca-Cusachs, J. M. Fernandez, and M. P. Sheetz. 2009. Stretching single talin rod molecules activates vinculin binding. *Science*. 323(5914):638-641, doi: 10.1126/science.1162912, https://www.ncbi.nlm.nih.gov/pubmed/19179532.
8. Winograd-Katz, S. E., R. Fässler, B. Geiger, and K. R. Legate. 2014. The integrin adhesome: from genes and proteins to human disease. *Nat Rev Mol Cell Biol*. 15(4):273-288, doi: 10.1038/nrm3769, https://www.ncbi.nlm.nih.gov/pubmed/24651544.
9. Nakao, N., K. Maki, M. R. K. Mofrad, and T. Adachi. 2019. Talin is required to increase stiffness of focal molecular complex in its early formation process. *Biochem Biophys Res Commun*. 518(3):579-583, doi: 10.1016/j.bbrc.2019.08.091, https://www.ncbi.nlm.nih.gov/pubmed/31451222.
10. Ghibaudo, M., A. Saez, L. Trichet, A. Xayaphoummine, J. Browaeys , P. Silberzan, A. Buguin, and B. Ladoux. 2008. Traction forces and rigidity sensing regulate cell functions. *Soft Matter*. 4(9):1836-1843.
11. Mekhdjian, A. H., F. Kai, M. G. Rubashkin, L. S. Prahl, L. M. Przybyla, A. L. McGregor, E. S. Bell, J. M. Barnes, C. C. DuFort, G. Ou, A. C. Chang, L. Cassereau, S. J. Tan, M. W. Pickup, J. N. Lakins, X. Ye, M. W. Davidson, J. Lammerding, D. J. Odde, A. R. Dunn, and V. M. Weaver. 2017. Integrin-mediated traction force enhances paxillin molecular associations and adhesion dynamics that increase the invasiveness of tumor cells into a three-dimensional extracellular matrix. *Mol Biol Cell*. 28(11):1467-1488, doi: 10.1091/mbc.E16-09-0654, https://www.ncbi.nlm.nih.gov/pubmed/28381423.

12. Hou, J. C., G. A. Shamsan, S. M. Anderson, M. M. McMahon, L. P. Tyler, B. T. Castle, R. K. Heussner, P. P. Provenzano, D. F. Keefe, V. H. Barocas, and D. J. Odde. 2019. Modeling distributed forces within cell adhesions of varying size on continuous substrates. *Cytoskeleton (Hoboken)*. 76(11-12):571-585, doi: 10.1002/cm.21561, https://www.ncbi.nlm.nih.gov/pubmed/31512404.
13. Sabass, B., and U. S. Schwarz. 2010. Modeling cytoskeletal flow over adhesion sites: competition between stochastic bond dynamics and intracellular relaxation. *J Phys Condens Matter*. 22(19):194112, doi: 10.1088/0953-8984/22/19/194112, https://www.ncbi.nlm.nih.gov/pubmed/21386438.
14. Bressloff, P. C. 2020. Stochastic resetting and the mean-field dynamics of focal adhesions. *Phys Rev E*. 102(2-1):022134, doi: 10.1103/PhysRevE.102.022134, https://www.ncbi.nlm.nih.gov/pubmed/32942383.
15. Bangasser, B. L., S. S. Rosenfeld, and D. J. Odde. 2013. Determinants of maximal force transmission in a motor-clutch model of cell traction in a compliant microenvironment. *Biophys J*. 105(3):581-592, doi: 10.1016/j.bpj.2013.06.027, https://www.ncbi.nlm.nih.gov/pubmed/23931306.
16. Bangasser, B. L., and D. J. Odde. 2013. Master equation-based analysis of a motor-clutch model for cell traction force. *Cell Mol Bioeng*. 6(4):449-459, doi: 10.1007/s12195-013-0296-5, https://www.ncbi.nlm.nih.gov/pubmed/24465279.
17. Chan, C. E., and D. J. Odde. 2008. Traction dynamics of filopodia on compliant substrates. *Science*. 322(5908):1687-1691, doi: 10.1126/science.1163595, https://www.ncbi.nlm.nih.gov/pubmed/19074349.
18. Bangasser, B. L., G. A. Shamsan, C. E. Chan, K. N. Opoku, E. Tüzel, B. W. Schlichtmann, J. A. Kasim, B. J. Fuller, B. R. McCullough, S. S. Rosenfeld, and D. J. Odde. 2017. Shifting the optimal stiffness for cell migration. *Nat Commun*. 8:15313, doi: 10.1038/ncomms15313, https://www.ncbi.nlm.nih.gov/pubmed/28530245.
19. Sens, P. 2013. Rigidity sensing by stochastic sliding friction. *Europhysics Letters*. 104(3):38003.